

REPORT DOCUMENTATION PAGE				Form Approved OMB No. 0704-0188	
Public reporting burden for this collection of information is estimated to average 1 hour per response, including the time for reviewing instructions, searching existing data sources, gathering and maintaining the data needed, and completing and reviewing the collection of information. Send comments regarding this burden estimate or any other aspect of this collection of information, including suggestions for reducing the burden, to Department of Defense, Washington Headquarters Services, Directorate for Information Operations and Reports (0704-0188), 1215 Jefferson Davis Highway, Suite 1204, Arlington, VA 22202-4302. Respondents should be aware that notwithstanding any other provision of law, no person shall be subject to any penalty for failing to comply with a collection of information if it does not display a currently valid OMB control number. PLEASE DO NOT RETURN YOUR FORM TO THE ABOVE ADDRESS.					
1. REPORT DATE (DD-MM-YYYY) 22-07-2010		2. REPORT TYPE Final Report		3. DATES COVERED (From – To) 22 July 2009 - 22-Jul-10	
4. TITLE AND SUBTITLE Light Pulse Interaction with Narrow Defects in Fiber Bragg Gratings				5a. CONTRACT NUMBER FA8655-09-1-3106	
				5b. GRANT NUMBER	
				5c. PROGRAM ELEMENT NUMBER	
6. AUTHOR(S) Professor Carlos Martel				5d. PROJECT NUMBER	
				5d. TASK NUMBER	
				5e. WORK UNIT NUMBER	
7. PERFORMING ORGANIZATION NAME(S) AND ADDRESS(ES) Universidad Politecnica de Madrid Plaza Cardenal Csineros 3 Madrid 28040 SPAIN				8. PERFORMING ORGANIZATION REPORT NUMBER N/A	
9. SPONSORING/MONITORING AGENCY NAME(S) AND ADDRESS(ES) EOARD Unit 4515 BOX 14 APO AE 09421				10. SPONSOR/MONITOR'S ACRONYM(S)	
				11. SPONSOR/MONITOR'S REPORT NUMBER(S) Grant 09-3106	
12. DISTRIBUTION/AVAILABILITY STATEMENT Approved for public release; distribution is unlimited.					
13. SUPPLEMENTARY NOTES					
14. ABSTRACT This report results from a contract tasking Universidad Politecnica de Madrid as follows: --Description of work The proposed research work will be carried out in 2 steps: (I) Formulation of the problem of light propagation on a FBG with a narrow defect in terms of the 1D Maxwell-Lorentz equations. Analysis and numerical computation of the reflection/transmission coefficients for the CME for different defect profiles. (II) Analysis of the pulse trapping/releasing characteristics of the defects: study of the internal defect modes and its excitability characteristics via light pulses.					
15. SUBJECT TERMS EOARD, Fibre Optics, Solitons, Nonlinear Optics					
16. SECURITY CLASSIFICATION OF:			17. LIMITATION OF ABSTRACT UL	18, NUMBER OF PAGES 64	19a. NAME OF RESPONSIBLE PERSON A. GAVRIELIDES
a. REPORT UNCLAS	b. ABSTRACT UNCLAS	c. THIS PAGE UNCLAS			19b. TELEPHONE NUMBER (Include area code) +44 (0)1895 616205

Light pulse interaction with narrow defects in fiber Bragg gratings

July 21, 2010

Final report to the European Office of Aerospace Research and Development

Research grant: FA8655-09-1-3106

Carlos Martel (carlos.martel@upm.es)

Depto. Fundamentos Matemáticos

E.T.S.I. Aeronáuticos

Universidad Politécnica de Madrid

28040 Madrid, SPAIN

Disclosure of inventions: I certify that there were no subject inventions to declare during the performance of this grant.

Carlos Martel (carlos.martel@upm.es)
Depto. Fundamentos Matemáticos
E.T.S.I. Aeronáuticos
Universidad Politécnica de Madrid
28040 Madrid, SPAIN

Table of Contents

List of Figures	4
Summary	5
Introduction	6
Methods, Assumptions, and Procedures	9
Asymptotic scaling of the defects	12
Narrow localized defects in FBG	16
Results and Discussion	25
Computation of the transmission/reflection coefficients	25
Nonlinear defect modes	29
Defect mode stability	34
Pulse trapping simulations	38
Numerical simulation of light propagation in a FBG with a defect	51
Conclusions	55
References	58
List of Symbols, Abbreviations, and Acronyms	60

List of Figures

Figure 1	One dimensional fiber with a perfectly periodic variation of the refractive index.	9
Figure 2	Refractive index dependence on the defect profile $f(x)$.	11
Figure 3	Asymptotic scaling of the profiles of $\alpha(x)$ in eq. (10): a) uniform, b) small periodic structure with period $2\pi/\beta$, c) slow defect, slow modulation of the small periodic structure, d) narrow localized defect with amplitude of the order of the small periodic structure, d) narrow localized defect with amplitude of order 1 centered around $x = 0$.	13
Figure 4	One dimensional fiber with a narrow defect in the periodic grating.	17
Figure 5	Sketch of the dispersion relation (18), with the resonant wavenumber $k = 1$ shown.	18
Figure 6	Sketch of the different asymptotic regions in the $x - t$ plane: (i) 1 and 2, away from the defect, where the NLCME applies, and (ii) the narrow shaded band of the defect in the vicinity of $x = 0$.	21
Figure 7	Sketch of the scattering problems that give the jump conditions at the defect: (a) outgoing wavetrain to the left with amplitude 1, and (b) outgoing wavetrain to the right with amplitude 1	22
Figure 8	Top: defect profile $f(x) = De^{-x^2}$, with $D \in [0, 1]$. Middle: modulus of the transmission and reflection coefficients. Bottom: phases of the transmission and reflection coefficients.	26
Figure 9	Top: defect profile $f(x) = De^{-x^2}$, with $D \in [-0.85, 0]$. Middle: modulus of the transmission and reflection coefficients. Bottom: phases of the transmission and reflection coefficients.	27
Figure 10	Top: defect profile $f(x) = -D(x + 1/3)e^{-x^2}$, with $D \in [0, 1]$. Middle: modulus of the transmission and reflection coefficients. Bottom: phases of the transmission and reflection coefficients.	28
Figure 11	Light intensity distribution of a DM localized at a defect at $X = 0$.	29
Figure 12	Standing GS profiles for $\theta = \pi/4, \pi/2$, and π . $H(X) = R(X)e^{i\phi(X)}$, modulus $R(X)$ (top plot) and phase $\phi(X)$ (bottom plot).	30
Figure 13	Construction of a DM joining two pieces of a standing GS.	31
Figure 14	Transmission, c_t , and reflection, c_r , coefficient size for the defect mode families DM1 and DM2.	32

Figure 15	Sketch of the profiles of the defect modes in families DM1 and DM2.	33
Figure 16	Stability of the DM1 family as a function of X_1 and ψ . Red dots indicate instability. The solution is also shown for three representative cases (marked with black dots). Top plots: spatial profiles of $ A^+ $ (blue line) and $ A^- $ (red line) at the end of the simulation, and the profile of the DM used as initial condition (black line). Bottom plots: temporal evolution of the norms $\ \frac{\partial}{\partial T} A_{1,2}^\pm \ $	36
Figure 17	Stability of the DM2 family as a function of X_1 and ψ . Red dots indicate instability. The solution is also shown for four representative cases (marked with black dots). Top plots: spatial profiles of $ A^+ $ (blue line) and $ A^- $ (red line) at the end of the simulation, and the profile of the DM used as initial condition (black line). Bottom plots: temporal evolution of the norms $\ \frac{\partial}{\partial T} A_{1,2}^\pm \ $	37
Figure 18	Left: moving Gap Soliton at $t = 0$, $A^+(A^-)$ thick (thin) line, with parameters $\sigma = \frac{1}{2}$, $\kappa = 1$, $c = \frac{1}{2}$ and $\theta = 2$. Right: domain of existence of the GS in the $c - \gamma$ plane (the dot corresponds to the GS shown).	39
Figure 19	DM1 defect interaction with a GS of speed $c = 0.2$ sent from the left. Bottom: $X - T$ diagram of the light intensity, $I = \sqrt{ A^+ ^2 + A^- ^2}$, during collision. Top: profiles of $ A^+ $ in blue and $ A^- $ in red at $T = 0$ (thin lines) and $T = 350$ (thick lines).	41
Figure 20	DM1 defect interaction with a GS of speed $c = 0.3$ sent from the left. Bottom: $X - T$ diagram of the light intensity, $I = \sqrt{ A^+ ^2 + A^- ^2}$, during collision. Top: profiles of $ A^+ $ in blue and $ A^- $ in red at $T = 0$ (thin lines) and $T = 300$ (thick lines).	42
Figure 21	DM1 defect interaction with a GS of speed $c = 0.4$ sent from the left. Bottom: $X - T$ diagram of the light intensity, $I = \sqrt{ A^+ ^2 + A^- ^2}$, during collision. Top: profiles of $ A^+ $ in blue and $ A^- $ in red at $T = 0$ (thin lines) and $T = 250$ (thick lines).	43
Figure 22	DM1 defect interaction with a GS of speed $c = 0.5$ sent from the left. Bottom: $X - T$ diagram of the light intensity, $I = \sqrt{ A^+ ^2 + A^- ^2}$, during collision. Top: profiles of $ A^+ $ in blue and $ A^- $ in red at $T = 0$ (thin lines) and $T = 200$ (thick lines).	44
Figure 23	DM1 defect interaction with a GS of speed $c = 0.6$ sent from the left. Bottom: $X - T$ diagram of the light intensity, $I = \sqrt{ A^+ ^2 + A^- ^2}$, during collision. Top: profiles of $ A^+ $ in blue and $ A^- $ in red at $T = 0$ (thin lines) and $T = 200$ (thick lines).	45
Figure 24	DM2 defect interaction with a GS of speed $c = 0.2$ sent from the left. Bottom: $X - T$ diagram of the light intensity, $I = \sqrt{ A^+ ^2 + A^- ^2}$, during collision. Top: profiles of $ A^+ $ in blue and $ A^- $ in red at $T = 0$ (thin lines) and $T = 350$ (thick lines).	46

Figure 25	DM2 defect interaction with a GS of speed $c = 0.3$ sent from the left. Bottom: $X - T$ diagram of the light intensity, $I = \sqrt{ A^+ ^2 + A^- ^2}$, during collision. Top: profiles of $ A^+ $ in blue and $ A^- $ in red at $T = 0$ (thin lines) and $T = 300$ (thick lines).	47
Figure 26	DM2 defect interaction with a GS of speed $c = 0.4$ sent from the left. Bottom: $X - T$ diagram of the light intensity, $I = \sqrt{ A^+ ^2 + A^- ^2}$, during collision. Top: profiles of $ A^+ $ in blue and $ A^- $ in red at $T = 0$ (thin lines) and $T = 250$ (thick lines).	48
Figure 27	DM2 defect interaction with a GS of speed $c = 0.5$ sent from the left. Bottom: $X - T$ diagram of the light intensity, $I = \sqrt{ A^+ ^2 + A^- ^2}$, during collision. Top: profiles of $ A^+ $ in blue and $ A^- $ in red at $T = 0$ (thin lines) and $T = 200$ (thick lines).	49
Figure 28	DM2 defect interaction with a GS of speed $c = 0.6$ sent from the left. Bottom: $X - T$ diagram of the light intensity, $I = \sqrt{ A^+ ^2 + A^- ^2}$, during collision. Top: profiles of $ A^+ $ in blue and $ A^- $ in red at $T = 0$ (thin lines) and $T = 200$ (thick lines).	50
Figure 29	Discretization of the spatial domain $[-L, L]$	52
Figure 30	Spatial profiles of the solution at $T=10$: $ A^+ $ (blue line) and $ A^- $ (red line). . . .	54
Figure 31	Modulus of the difference between two increasingly refined solutions at $T=10$. Blue line for A^+ and red for A^-	54

Summary

This is the final report of the research grant FA8655-09-1-3106 issued by the European Office of Aerospace Research and Development. This research effort is devoted to the analysis of the weakly nonlinear description of light interaction with narrow defects in fiber Bragg gratings. In particular it includes: (i) the derivation of the appropriate envelope equation description that takes into account the effect of the grating defect, starting from the full 1D Maxwell-Lorentz equations, (ii) the analysis and the numerical computation of the resulting reflection/transmission coefficients induced by different defect profiles, (iii) the derivation of a family of nonlinear standing defect modes that keep light confined to the vicinity of the defect, (iv) the development of a numerical code for the simulation of the time evolution of the complete problem of light propagation in a fiber Bragg grating with a sharp defect, (v) the numerical analysis of the stability properties of the nonlinear defect modes, and (vi) the numerical exploration of the pulse trapping characteristics for some typical defects.

Introduction

Data is carried as light pulses in optical communication systems. A very high reduction in the communication speed rate comes from the need to perform the processing of the signal electronically. It is therefore very interesting to try to find new materials and optical structures that can perform all signal processing optically, bypassing the need for the optical/electronic interface. To this end, we have seen in the past years an increasing research activity devoted to the study of optical nonlinearities and light interaction with nonuniformities, in an effort to look for new physical effects that can be applied in the design of efficient all-optical switching and storing devices.

One of the most promising optical configurations are fiber Bragg gratings (FBG). FBG are microstructured optical fibers that present a spatially periodic variation of the refractive index along the length of the fiber. The reflection produced by the grating induces a nontrivial coupling between the forward and backward propagating light beams when their frequency is at or near resonance. This effect, combined with the Kerr nonlinearity of the fiber that appears for high intensity pulses, results in the very particular light propagation characteristics of these devices, which makes them very interesting for various technological applications that range from fiber sensing to all-optical communication (see [1] and [2] for a general description of FBG).

FBG support the propagation of the so-called Gap solitons (GS), which are a family of localized nonlinear light pulses that propagate over the periodic grating. GS are not true solitons, since their dynamics is not completely integrable, but they can be stable and propagate without distortion along the FBG. Standard solitons in a bare fiber come out of the balance of nonlinearity and dispersion [3], and this balance can take lengths up to several kilometers to be realized. In the case of GS this characteristic formation length can be reduced to a few centimeters. This is because GS result from a completely different balance that includes propagation at the group velocity, grating reflection, and nonlinearity. Furthermore, GS have the amazing property that they can travel at any speed between zero and the speed of light of the bare fiber. This possibility to have “slow light” or “trapped light” inside small FBG devices has made them extremely promising for the manufacturing of all-optical buffers and storing devices, and have fueled numerous studies on GS

dynamics and stability in FBG in the past 15 years (see, e.g., [4, 5, 6, 7] for reviews, and [8] for a recent experimental realization).

More recently a new strategy for trapping light inside FBG has been proposed that consists of introducing a defect or inhomogeneity in the periodic grating. The idea is to send a moving GS that, after interacting with the defect in the grating, ends up trapped in the form of a stable pulse of standing light localized around the defect.

The possibility of trapping a GS at a grating defect depends on the particular details of the defect and, basically, two asymptotically different configurations have been analyzed: slow defects and narrow defects. Here we call slow defects to those that consist of a modulation of the periodic grating on a scale that is much larger than the period of the grating. And, on the other hand, narrow defects correspond to distortions of the grating intensity with a typical length scale of a few periods of the grating.

For slow grating defects, the problem of GS trapping and releasing has been analyzed in several papers in the recent years [9, 10, 11, 12, 13, 14]. All these analysis are theoretical and numerical, and have been performed within the scope of the Nonlinear Coupled Mode Equations (NLCME) formalism. The NLCME are a set of two coupled envelope equations that describe the weakly nonlinear dynamics of light propagation in a FBG of small intensity (see, e.g., [15] and references therein). The presence of the slow modulation of the grating gives rise to a spatial dependence of the linear reflection coefficients of the NLCME, which are constant for a perfectly uniform periodic grating. The analysis of the characteristics of a given family of defects starts with the computation of the defect modes, which are standing light pulses localized at the defect. The defect modes are first computed in the linearized version of the NLCME for small light intensity and then extended to higher intensity values using nonlinear continuation techniques. Once the nonlinear defect modes are computed, one has to tune the defect parameters in order to find the stable ones, which are the only valid candidates for captured light pulses. And finally, the transfer of energy from an incoming GS to a stable defect mode is typically analyzed through the numerical simulation of the dynamics of the complete process using the variable coefficient NLCME. Following these steps, GS trapping defects have been located in the above references that can give rise, at least within the scope of the theoretical

model, to capture standing light pulses inside a FBG.

The case of narrow defects is, we believe, much more realistic from a manufacturing point of view than the previous slow modulation defect, but has not been so far studied in that much detail. The analysis that can be found in the literature uses the NLCME with some Dirac delta terms added to somehow take into account the localized effect of a narrow defect (see, e.g., [16, 17, 18]). These terms are added in a completely heuristic way, just to try to qualitatively reproduce the dynamics of the process, and they have no connection with the actual shape of the grating distortion.

The purpose of this research work is to take a closer look into the interaction of light with this kind of narrow defects in FBG, and it is organized as follows.

In the first part (Methods, Assumptions, and Procedures) we begin with a discussion of the correct asymptotic scaling that the localized defects must have in order to appear as a first order effect in the NLCME formalism. We then show, in the next section, that, from the point of view of the slow scale description, a narrow defect manifests itself as an internal interface inside the perfectly periodic FBG. The resulting transmission and reflection coefficients across this interface depend on the particular shape of the defect, and, from the full 1D Maxwell equations for light propagation, we derive the scattering problem that determines the values of the coefficients.

The second part (Results and Discussion) presents, in the first section, some numerical solutions of the scattering problem, showing the transmission and reflection coefficients induced by several simple defect profiles. In the following section we introduce a family of localized, standing nonlinear defect modes that keep light confined to the vicinity of the defects. These defect modes depend on the particular values of the coefficients of the defect, that is, on the particular details of the narrow defect profile. In the two subsequent sections we analyze numerically the stability of these nonlinear defect modes, and, for two representative stable defect modes, we explore the possibility of light pulse trapping (i.e., the possibility of exciting the standing defect modes by sending moving pulses to collide with them). The final section of this second part is dedicated to present the details of the numerical code used for the computation of the temporal evolution of the system. And finally, this report ends with a summary of the obtained results listed in the Conclusions.

Methods, Assumptions, and Procedures

For the case of a fiber with a perfectly periodic grating and a cubic Kerr nonlinearity, we will use as a model for light propagation the one-dimensional Maxwell's equations [1] for the electromagnetic fields evolution together with an anharmonic Lorentz oscillator model for the polarization (see e.g. [9, 19] and references therein),

$$\frac{\partial B}{\partial t} = \frac{\partial E}{\partial x}, \quad (1)$$

$$\mu_0 \frac{\partial D}{\partial t} = \frac{\partial B}{\partial x}, \quad (2)$$

$$D = \epsilon_0 E + P, \quad (3)$$

$$\Omega_p^{-2} \frac{\partial^2 P}{\partial t^2} + (1 - 2\Delta n \cos(2\pi x/\lambda_g))P - \gamma P^3 = \epsilon_0 \chi E. \quad (4)$$

In the system above, the electric field E , the magnetic field B , the dielectric displacement D , and the polarization P are scalar fields that depend on time t and on the spatial variable x that runs along the fiber. The permeability and the permittivity of the vacuum are denoted by μ_0 and ϵ_0 , respectively. The characteristic frequency Ω_p accounts for the non instantaneous polarization response of the media, Δn and λ_g represent the strength and the period of the grating, that is, the strength and the period of the spatial periodic variation of the refractive index of the fiber (Δn measures the size of the nonuniformities of the refraction index relative to its mean value n_0 , see Fig. 1), χ is the linear polarizability of the medium ($n_0^2 = 1 + \chi$) and $\gamma > 0$ is the coefficient of the nonlinear Kerr effect.

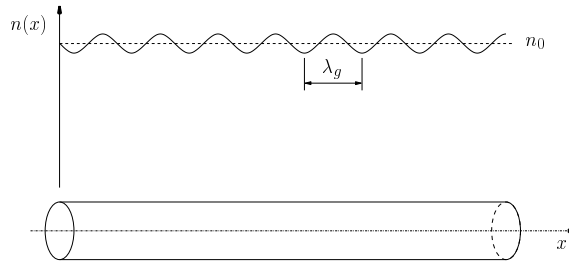


Figure 1: One dimensional fiber with a perfectly periodic variation of the refractive index.

In order to simplify subsequent calculations it is convenient to make the system

(1)-(4) non dimensional using the following rescalings:

$$B = \sqrt{\mu_0/(\epsilon_0\gamma)}\tilde{B}, \quad D = (1/\sqrt{\gamma})\tilde{D}, \quad E = (1/\sqrt{(\epsilon_0\gamma)})\tilde{E}, \quad P = (1/\sqrt{\gamma})\tilde{P},$$

$$x = (\lambda_g/\pi)\tilde{x}, \quad t = (\lambda_g/c\pi)\tilde{t},$$

here $c^2 = 1/(\epsilon_0\mu_0)$ is the vacuum speed of light. After dropping tildes, the nondimensional Maxwell-Lorentz equations (MLE hereafter) can be written as

$$\frac{\partial B}{\partial t} = \frac{\partial E}{\partial x}, \tag{5}$$

$$\frac{\partial D}{\partial t} = \frac{\partial B}{\partial x}, \tag{6}$$

$$D = E + P, \tag{7}$$

$$\omega_p^{-2} \frac{\partial^2 P}{\partial t^2} + (1 - 2\Delta n \cos(2x))P - P^3 = (n_0^2 - 1)E, \tag{8}$$

where the dimensionless finite time polarization response frequency is now $\omega_p^2 = \Omega_p^2 \lambda_g^2 / (c^2 \pi^2)$. Notice that we have rescaled the spatial variable x to make wavenumber of the grating equal to 2 (see eq. (8)). As we will see below, the reason for this choice is that the wavetrains that resonate with the grating and develop along the fiber will then have wavenumber 1. We have also used the rescaling to absorb the vacuum properties ϵ_0 and μ_0 (the vacuum speed of light is now equal to 1 in the rescaled variables) and the nonlinear coefficient γ .

The periodic structure of the fiber appears in the spatial dependence of the potential of the anharmonic Lorentz oscillator model for the polarization response of the media given by eq. (8). In order to take into account the possibility of a defect in the grating, we change it to

$$\omega_p^{-2} \frac{\partial^2 P}{\partial t^2} + (1 + f(x))P - P^3 = (n_0^2 - 1)E, \tag{9}$$

where $f(x)$ is a real function that accounts for a more general spatial nonuniformity.

Note that for the simplified case of linear light propagation with instantaneous polarization response ($\omega_p \rightarrow \infty$),

- if there is no spatial structure, $f(x) = 0$, then we obtain from eq. (9) $P =$

$(n_0^2 - 1)E$, which once inserted into eqs. (5)-(7) gives

$$n_0^2 \frac{\partial^2 E}{\partial t^2} = \frac{\partial^2 E}{\partial x^2},$$

and we recover the standard equations for linear light propagation in a bare fiber with uniform refractive index n_0 .

- Also, if $f(x) = -2\Delta n \cos(2x)$ with $|\Delta n| \ll 1$, then we obtain

$$(n_0^2 + 2\Delta n \cos(2x)(n_0^2 - 1) + \dots) \frac{\partial^2 E}{\partial t^2} = \frac{\partial^2 E}{\partial x^2},$$

that corresponds to a perfectly periodic spatial modulation of the refractive index of small amplitude, proportional to $\Delta n \ll 1$, like the one depicted in Fig. 1.

- And finally, narrow defects can be taken into account just by allowing $f(x)$ to exhibit a more general profile localized in a spatial region of characteristic size $\delta_d \sim 1$ (recall that, with the nondimensionalization that we have used, the period of the grating is equal to 2). The resulting effective refractive index is then given by

$$n^2 = n_0^2 \left(\frac{1 + f(x)/n_0^2}{1 + f(x)} \right),$$

where a positive (negative) value $f(x)$ results in a local decrease (increase) of n^2 , see Fig. 2.

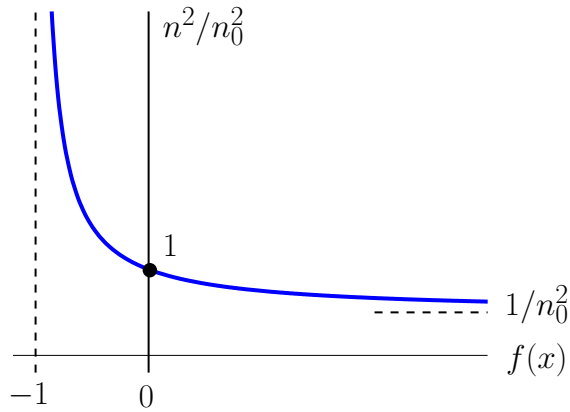


Figure 2: Refractive index dependence on the defect profile $f(x)$.

Asymptotic scaling of the defects

Before going into the general MLE formulation we discuss the different possibilities for the asymptotic scalings of the defects and how they translate into the resulting envelope equations using a much simpler model that retains all qualitative features of resonant wave propagation on a periodic grating with defects.

Our toy model is the following simple linear conservative oscillator

$$\frac{\partial^2 E}{\partial x^2} + \alpha(x)^2 E = 0, \quad (10)$$

where we allow the local wavenumber $\alpha(x)$ to depend on the spatial variable x . We are going to consider different $\alpha(x)$ distributions (see Fig. 3) and look for the corresponding slow scale envelope equations.

Case 0 For the trivial case of uniform $\alpha(x) = \alpha_0 \sim 1$ (Fig. 3a), the exact solution of eq. (10) is a pure harmonic with wavenumber α_0

$$E = A_0 e^{i\alpha_0 x} + \text{c.c.},$$

where A_0 is a complex constant, and c.c. stands for the complex conjugate.

Case 1 If we now add a small periodic structure with wavenumber β : $\alpha^2(x) = \alpha_0^2(1 + \varepsilon \cos(\beta x))$ with $0 \leq \varepsilon \ll 1$ and $0 < \alpha_0, \beta \sim 1$ (Fig. 3b), then its effect is to introduce a slow modulation of the amplitude A_0 that evolves in a much longer spatial scale $X = \varepsilon x$. This slow modulation can be easily captured using standard asymptotic perturbation techniques [20, 21]. The solution is expanded as

$$E = E_0(x, X) + \varepsilon E_1(x, X) + \dots,$$

which once inserted into eq.(10) gives, at order ε^0 ,

$$\frac{\partial^2 E_0}{\partial x^2} + \alpha_0^2 E_0 = 0 \quad \rightarrow \quad E_0 = A_0(X) e^{i\alpha_0 x} + \text{c.c.}.$$

At order ε^1 we obtain

$$\frac{\partial^2 E_1}{\partial x^2} + \alpha_0^2 E_1 = -[2i\alpha_0 \frac{dA_0}{dX} e^{i\alpha_0 x} + \alpha_0^2 \cos(\beta x) A_0 e^{i\alpha_0 x} + \text{c.c.}] = \text{RHS},$$

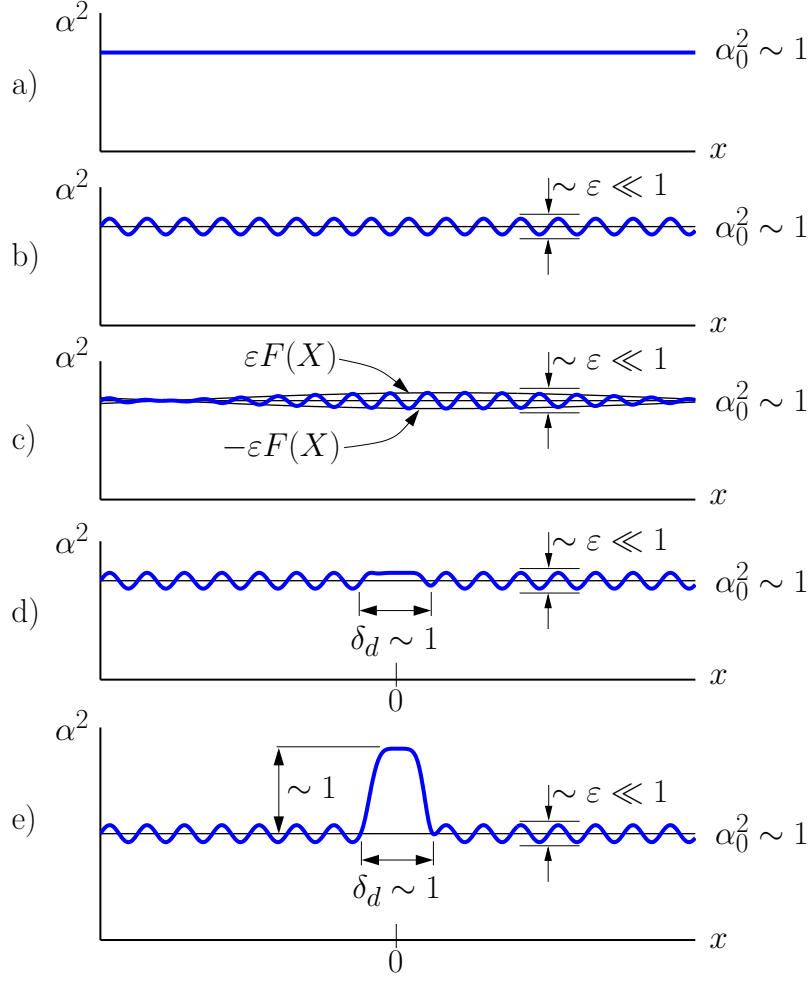


Figure 3: Asymptotic scaling of the profiles of $\alpha(x)$ in eq. (10): a) uniform, b) small periodic structure with period $2\pi/\beta$, c) slow defect, slow modulation of the small periodic structure, d) narrow localized defect with amplitude of the order of the small periodic structure, e) narrow localized defect with amplitude of order 1 centered around $x = 0$.

where RHS stands for right hand side terms. In order for E_1 to be bounded in the fast scale x , the following solvability condition must be satisfied

$$\lim_{L \rightarrow \infty} \frac{1}{2L} \int_{-L}^L \text{RHS} e^{-i\alpha_0 x} dx = 0,$$

which gives the evolution of the amplitude A_0 in the slow scale X :

$$\begin{aligned} 2i\alpha_0 \frac{dA_0}{dX} &= 0 \quad \text{for } \beta \neq 2\alpha_0, \text{ and} \\ 2i\alpha_0 \frac{dA_0}{dX} + \frac{\alpha_0^2}{2} A_0 &= 0 \quad \text{for } \beta = 2\alpha_0, \end{aligned}$$

where we have taken into account that $\cos(\beta x) = (e^{i\beta x} + e^{-i\beta x})/2$, and that $\alpha_0, \beta > 0$. Note that only in the resonant case $\beta = 2\alpha_0$ there is an order one effect of the small periodic structure in the amplitude of the solution A_0 . For the non-resonant case $\beta \neq 2\alpha_0$, the resulting equation, at first order, is the same as in Case 0, where there were no periodic structure.

Case 2 In the resonant case, the addition of a slow scale modulation to the amplitude of the small periodic structure, $\alpha^2(x) = \alpha_0^2(1 + \varepsilon F(X) \cos(2\alpha_0 x))$ with $0 \leq \varepsilon \ll 1$, $0 < \alpha_0 \sim 1$, and $|F| \sim 1$ and (Fig. 3c), just produces an evolution equation for A_0 completely similar to that in the previous case but with a coefficient that depends on X :

$$2i\alpha_0 \frac{dA_0}{dX} + \frac{\alpha_0^2}{2} F(X) A_0 = 0$$

This case corresponds to the slow defects in FBG, which are described by a NLCME but with variable linear reflection coefficients that inherit the slow modulation present in the grating [9, 10, 11, 12, 13, 14].

Case 3 A narrow distortion of the periodic resonant structure can be modeled as $\alpha^2(x) = \alpha_0^2(1 + \varepsilon(1 + f(x)) \cos(2\alpha_0 x))$ with $0 \leq \varepsilon \ll 1$ and $0 < \alpha_0 \sim 1$, where the real function $f(x)$ is zero everywhere except in the narrow defect region of length $\delta_d \sim 1$ where $|f(x)| \sim 1$, see Fig. 3d. The corresponding evolution equation for A_0 can be obtained proceeding as in Case 1. The right hand side terms of the equation for the correction E_1 can be written as

$$\text{RHS} = -[2i\alpha_0 \frac{dA_0}{dX} e^{i\alpha_0 x} + \alpha_0^2((1 + f(x))) \cos(2\alpha_0 x) A_0 e^{i\alpha_0 x} + \text{c.c.}],$$

and the solvability condition now gives

$$2i\alpha_0 \frac{dA_0}{dX} + \frac{\alpha_0^2}{2} A_0 + \alpha_0^2 \lim_{L \rightarrow \infty} \frac{1}{2L} \int_{-L}^L f(x) \cos(2\alpha_0 x) (A_0 e^{i\alpha_0 x} + \text{c.c.}) e^{-i\alpha_0 x} dx = 0.$$

Since $f(x)$ is zero everywhere except in the narrow defect region, the integral above is bounded, and the limit as $L \rightarrow \infty$ is zero. The resulting equation for the slow modulation of A_0 is the same as in Case 1, and thus a narrow defect in a small periodic structure as the one depicted Fig. 3d produces no effect at all at first order.

Case 4 The only way for a narrow localized defect to be felt at leading order is to have a much higher distortion amplitude; of order one, see Fig. 3e. In this case we can write $\alpha^2(x) = \alpha_0^2(1 + f(x) + \varepsilon \cos(2\alpha_0 x))$ with $0 \leq \varepsilon \ll 1$, $0 < \alpha_0 \sim 1$, and the real function $f(x)$ is again zero everywhere except in the narrow defect region of length $\delta_d \sim 1$ centered around $x = 0$ where $|f(x)| \sim 1$. Away from the localized defect the structure recovers its periodicity and the envelope equation obtained in Case 1 describes the slow modulation of A_0 . So, if we call A_1 and A_2 to the first order amplitudes of the solution in the regions at the left and right of the defect, we have:

$$2i\alpha_0 \frac{dA_1}{dX} + \frac{\alpha_0^2}{2} A_1 = 0 \quad \text{for } X < 0, \quad \text{and} \quad (11)$$

$$2i\alpha_0 \frac{dA_2}{dX} + \frac{\alpha_0^2}{2} A_2 = 0 \quad \text{for } X > 0. \quad (12)$$

From the point of view of the slow scale X the defect is seen as a sharp interface of zero thickness. In order to get the jump conditions across this interface we have to study the internal problem, which is given by eq. (10),

$$\frac{\partial^2 E}{\partial x^2} + \alpha_0^2(1 + f(x))E = 0, \quad (13)$$

where, in first approximation, we have neglected the effect of the small grating inside the defect. This equation has to be solved with the boundary

condition

$$E \rightarrow e^{i\alpha_0 x} + \text{c.c.} \quad \text{as } x \rightarrow -\infty,$$

and, as an output, one gets the behavior to the right of the defect

$$E \rightarrow c_d e^{i\alpha_0 x} + \text{c.c.} \quad \text{as } x \rightarrow +\infty.$$

Once this scattering problem is solved we can write the jump condition across the defect

$$A_2 = c_d A_1 \quad \text{at } X = 0. \quad (14)$$

This condition together with eqs. (11) and (12) completes the description of the slow scale dynamics of eq. (10) for a small resonant structure with a narrow defect. Note that, for the computation of the jump condition coefficient c_d , the detailed knowledge of the defect is essential, and the small periodic structure is not relevant since it is of higher order as compared to the order one amplitude of the defect. It is also worth to mention that the problem inside the defect given by eq. (13) appears to be as complicated as the original problem (10), and one could be tempted to conclude that no simplification comes out of this asymptotic perturbation analysis. Well, this is obviously not true, since in problem (10) we have a short spatial scale $x \sim 1$ that has to be integrated accurately to very long distances of the order $x \sim 1/\varepsilon \gg 1$ (i.e., $X \sim 1$), while in the long scale description given by eqs. (11), (12) and (14) there is only one spatial scale $X \sim 1$ and its integration is numerically much cheaper.

Narrow localized defects in FBG

Now that the required asymptotic scaling of narrow localized defect has been made clear in the previous section we can go back to our original FBG problem. For the sake of completeness we repeat here the MLE formulation for a FBG with a narrow defect that we are going to use:

$$\frac{\partial^2(E + P)}{\partial t^2} = \frac{\partial^2 E}{\partial x^2}, \quad (15)$$

$$\frac{\partial^2 P}{\partial t^2} = -\omega_p^2(1 - 2\Delta n \cos(2x) + f(x))P + \omega_p^2(n_0^2 - 1)E + \omega_p^2 P^3. \quad (16)$$

These are just the nondimensional equations (5)-(8) after elimination of the dielectric displacement D and the magnetic field B . We are interested in deriving the envelope equations for the long scale, weakly nonlinear dynamics of this system, $|E|, |P| \ll 1$, for the case of a small amplitude periodic grating, $\Delta n \ll 1$, and when there is a narrow defect of extension $\delta_d \sim 1$ given by the localized function $f(x)$ with order one amplitude (see Fig. 4).

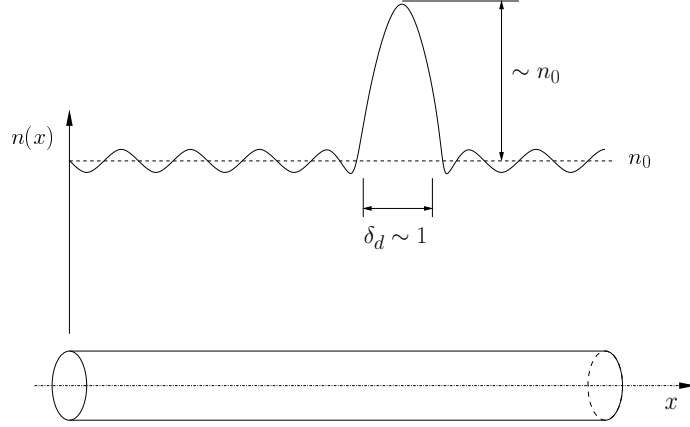


Figure 4: One dimensional fiber with a narrow defect in the periodic grating.

Region away from the defect

To the left and right of the defect the grating is perfectly periodic, and the appropriate envelope equations in these regions are the standard NLCME. We briefly sketch here the derivation of the NLCME (for a detailed account of this process see, e.g., [15, 22]).

The linear propagation characteristics of the system (15)-(16) are obtained by looking for uniform wavetrain solutions with spatial wavenumber k and frequency ω_k ,

$$\begin{Bmatrix} E(x, t) \\ P(x, t) \end{Bmatrix} = \begin{Bmatrix} E_k \\ P_k \end{Bmatrix} e^{ikx + i\omega_k t} + \text{c.c.}, \quad (17)$$

in the linearized version of the system (15)-(16) for the bare fiber (i.e., in the absence of grating or defects). The resulting dispersion relation is of the form (see Fig. 5):

$$\omega_k = \pm \sqrt{(k^2 + \omega_p^2 n_0^2)/2 \pm \sqrt{(k^2 + \omega_p^2 n_0^2)^2/4 - \omega_p^2 k^2}}, \quad (18)$$

with associated eigenvectors,

$$\begin{Bmatrix} E_k \\ P_k \end{Bmatrix} = \begin{Bmatrix} \omega_k^2 \\ k^2 - \omega_k^2 \end{Bmatrix} \quad (19)$$

Note that there are two very different behaviors for large wavenumbers: one dominated by the finite time polarization response of the medium, $\omega_k \rightarrow \pm\omega_p$ as $k \rightarrow \pm\infty$, and a second one, $\omega_k \rightarrow \pm k$ as $k \rightarrow \pm\infty$, which corresponds to propagation like in the vacuum with small polarization effects.

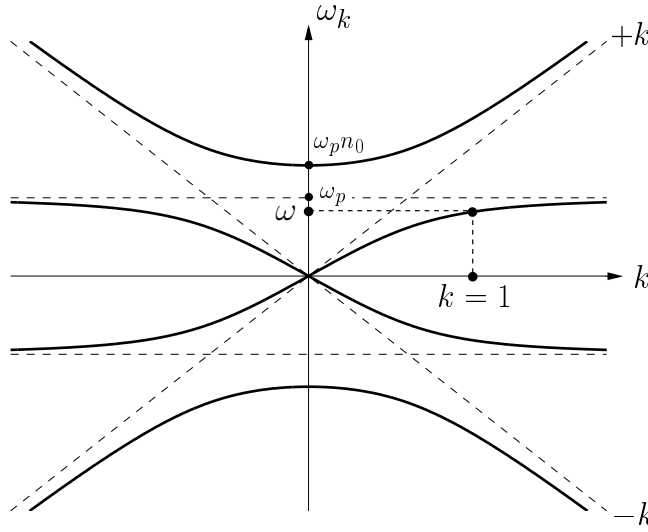


Figure 5: Sketch of the dispersion relation (18), with the resonant wavenumber $k = 1$ shown.

The weakly nonlinear response of the system when a small periodic grating is present can be described with two counterpropagating, slowly modulated wavetrains

$$\begin{Bmatrix} E(x, t) \\ P(x, t) \end{Bmatrix} = V_0(A^+(x, t)e^{ix+i\omega t} + A^-(x, t)e^{-ix+i\omega t}) + \text{c.c.} + \dots, \quad (20)$$

which have wavenumbers and frequency

$$k = \pm 1 \quad \text{and} \quad \omega_k = \omega = \sqrt{(1 + \omega_p^2 n_0^2)/2 \pm \sqrt{(1 + \omega_p^2 n_0^2)^2/4 - \omega_p^2}}, \quad (21)$$

and resonate with the grating (recall that the grating wavenumber is 2). The eigen-

vector V_0 is given by

$$V_0 = \begin{Bmatrix} \omega^2 \\ 1 - \omega^2 \end{Bmatrix},$$

and the weakly nonlinear level of this approach requires essentially that

$$\dots \ll |A_{xx}^\pm| \ll |A_x^\pm| \ll |A^\pm| \ll 1, \quad \dots \ll |A_t^\pm| \ll |A^\pm| \ll 1 \quad \text{and} \quad \Delta n \ll 1, \quad (22)$$

that is, small amplitudes that depend slowly on space and time, and small grating strength.

Once we take the ansatz (20) to the system equations eqs. (15)-(16) and apply solvability conditions to ensure the boundedness of the solution in the fast spatial and temporal scales, we arrive to the well known NLCME for the evolution of the amplitudes A^\pm

$$A_t^+ = v_g A_x^+ + w \Delta n A^- + A^+ (u_1 |A^+|^2 + u_2 |A^-|^2) + \dots, \quad (23)$$

$$A_t^- = -v_g A_x^- + w \Delta n A^+ + A^- (u_1 |A^-|^2 + u_2 |A^+|^2) + \dots, \quad (24)$$

where v_g is the group velocity

$$v_g = \left. \frac{d\omega_k}{dk} \right|_{k=1} = \frac{\omega(\omega^2 - \omega_p^2)}{\omega^4 - \omega_p^2}, \quad (25)$$

w is the coefficient of the effect of the grating

$$w = i \frac{\omega(1 - \omega^2)}{2(\omega^4 - \omega_p^2)} \omega_p^2, \quad (26)$$

and the nonlinear terms are given by

$$u_1 = i \frac{3\omega(1 - \omega^2)^3}{2(\omega^4 - \omega_p^2)} \omega_p^2 \quad \text{and} \quad u_2 = i \frac{3\omega(1 - \omega^2)^3}{(\omega^4 - \omega_p^2)} \omega_p^2. \quad (27)$$

If we introduce the slow scale $L \sim 1/\Delta n \gg 1$, and rescale space, time and the amplitudes

$$x = LX, \quad t = (L/v_g)T, \quad \overline{A^\pm} = \sqrt{v_g/(L|u_2|)} \tilde{A}^\pm, \quad (28)$$

we arrive, after dropping tildes, to the scaled standard NLCME

$$A_T^+ - A_X^+ = i\kappa A^- + iA^+(\sigma|A^+|^2 + |A^-|^2), \quad (29)$$

$$A_T^- + A_X^- = i\kappa A^+ + iA^-(\sigma|A^-|^2 + |A^+|^2), \quad (30)$$

where, in order to make the nonlinear and grating coefficients positive, we have changed to the complex conjugates of the amplitudes. The scaled grating strength $\kappa = \Delta n L |w| / v_g \sim 1$ is always positive, and the nonlinear coefficient $\sigma = \frac{1}{2}$.

The NLCME (29)-(30) give the slow time, long scale evolution of light propagation in a FBG, and represent a balance of the transport at the group velocity, the effect of the grating, and the cubic Kerr nonlinearity. This hyperbolic system and its more remarkable solutions have been widely studied theoretically and numerically, see e.g. [23, 6, 15, 24, 22] and references therein. As sketched in Fig. 6, the NLCME are valid in the perfectly periodic grating regions 1 and 2, to the left and right of the defect, respectively. In order to complete the formulation of the problem we have to study the narrow defect region near $x = 0$ to obtain the appropriate jump conditions that would prescribe the value of the outgoing envelopes, A_1^+ and A_2^- , in terms of the incoming ones A_1^- and A_2^+ , see Fig. 6.

Jump conditions at a narrow defect

In the narrow region near the defect $x \sim 1$, the profile $|f(x)| \sim 1$ in the MLE (15)-(16), and the problem can be simplified to

$$\begin{aligned} \frac{\partial^2(E + P)}{\partial t^2} &= \frac{\partial^2 E}{\partial x^2}, \\ \frac{\partial^2 P}{\partial t^2} &= -\omega_p^2(1 + f(x))P + \omega_p^2(n_0^2 - 1)E, \end{aligned}$$

where, in first approximation, we have neglected the small nonlinearities and the small grating effects. In order to match with the resonant wavetrains in regions 1 and 2 away from the defect (see Fig. 6), we look for solutions of this linear system of the form $(E, P) = (a(x), b(x))e^{i\omega t}$. After eliminating $b(x)$ we end up with a second

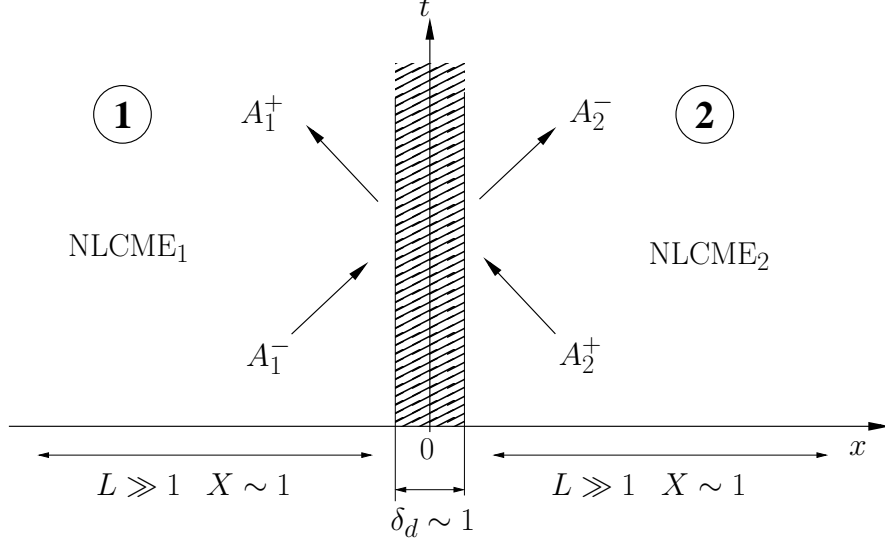


Figure 6: Sketch of the different asymptotic regions in the $x-t$ plane: (i) 1 and 2, away from the defect, where the NLCME applies, and (ii) the narrow shaded band of the defect in the vicinity of $x = 0$.

order ordinary differential equation for $a(x)$ that can be written as

$$\frac{d}{dx} \begin{bmatrix} a \\ a_x \end{bmatrix} = \begin{bmatrix} 0 & 1 \\ -\omega^2 \frac{\frac{\omega_p^2}{\omega^2} - (n_0^2 + f(x))}{\frac{\omega_p^2}{\omega^2} - (1 + f(x))} & 0 \end{bmatrix} \begin{bmatrix} a \\ a_x \end{bmatrix}. \quad (31)$$

Note that the detail of the periodic grating is only present in the equation above in the frequency ω , which is selected through the wavenumbers $k = \pm 1$ that resonate with the grating (see eq. (21)). As it is shown in Fig. 5, we choose ω on the lower branch of the dispersion relation. This lower branch is the one that, as $\omega_p \rightarrow \infty$, gives the frequently used instantaneous polarization limit.

Away from the defect, as $x \rightarrow \pm\infty$, $f(x) \rightarrow 0$, and the system (31) becomes a constant coefficient problem whose solution behaves as

$$a(x) \sim a^+ e^{ix} + a^- e^{-ix}. \quad (32)$$

The propagation characteristics of the bare fiber are thus recovered, and the coefficients a^+ and a^- have to match with the left and right going envelopes A^+ and A^-

of the regions 1 and 2 in Fig. 6.

To evaluate the jump conditions at the defect we have to solve the two scattering problems depicted in Fig. 7, which correspond to the determination of the amplitude of the wavetrains $e^{\pm ix}$ that we require at $x \rightarrow \pm\infty$ in order to produce amplitude 1 for e^{ix} as $x \rightarrow -\infty$ (Fig. 7a), and amplitude 1 for e^{-ix} as $x \rightarrow +\infty$ (Fig. 7b).

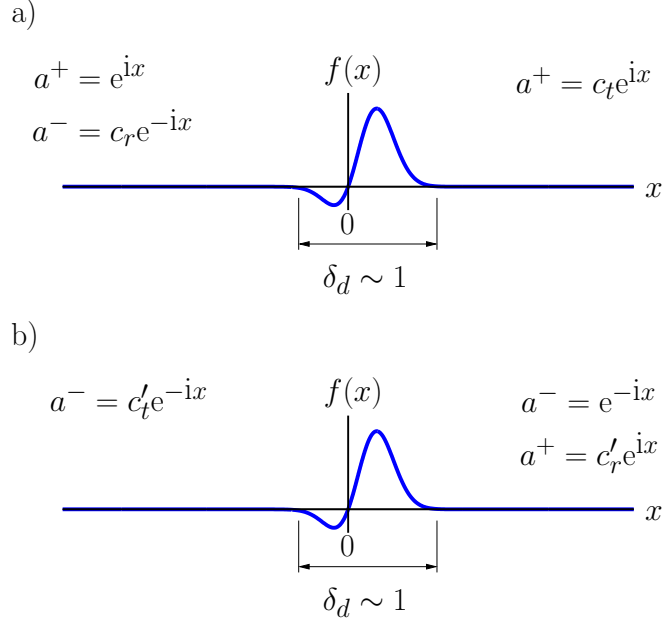


Figure 7: Sketch of the scattering problems that give the jump conditions at the defect: (a) outgoing wavetrain to the left with amplitude 1, and (b) outgoing wavetrain to the right with amplitude 1

The boundary conditions for the problem in Fig. 7a are

$$\begin{aligned} x \rightarrow -\infty, \quad a &\rightarrow e^{ix} + c_r e^{-ix}, \quad \text{and} \\ x \rightarrow \infty, \quad a &\rightarrow c_t e^{ix}, \end{aligned}$$

which correspond to a wavetrain of amplitude 1 outgoing to the left, and to no outgoing wave to the right. In order to extract the exponential components of the solution, we multiply the solution by the corresponding left eigenvectors of the constant matrix of the system (31) that is obtained for $x \rightarrow \pm\infty$ (see, e.g., [25]). The left eigenvectors are given by

$$[\pm i, 1] \quad \text{for} \quad e^{\pm ix},$$

and the above boundary conditions can be transformed into

$$x \rightarrow -\infty, \quad ia + a_x \rightarrow 2ie^{ix}, \quad \text{and} \quad (33)$$

$$x \rightarrow \infty, \quad ia - a_x \rightarrow 0, \quad (34)$$

which are much more convenient from the point of view of the numerical solution of the problem.

Once the scattering problem (31) with the boundary conditions (33) and (34) is solved, the reflection and transmission coefficients can be obtained from the limits

$$x \rightarrow -\infty, \quad ia - a_x \rightarrow 2ic_r e^{-ix}, \quad \text{and} \quad (35)$$

$$x \rightarrow \infty, \quad ia + a_x \rightarrow 2ic_t e^{ix}. \quad (36)$$

The problem (31) has real coefficients so, for any complex solution $[a, a_x]$, the complex conjugate $[\bar{a}, \bar{a}_x]$ is another, linearly independent, solution. On the other hand, the trace of the matrix of the system is zero (i.e., it is conservative) and therefore the determinant of the fundamental matrix composed by the two solutions $[a, a_x]$ and $[\bar{a}, \bar{a}_x]$ has to be constant (see, e.g., [26]):

$$\frac{d}{dx}(a\bar{a}_x - \bar{a}a_x) = 0,$$

which, for the scattering problem in Fig. 7a, gives the following relation

$$|c_t|^2 + |c_r|^2 = 1. \quad (37)$$

This equation just states the fact that the light propagation model given by eqs. (15) and (16) is conservative, and thus all the light intensity sent into the defect by the incoming beam has to come out in the reflected and transmitted beams.

Moreover, the solution of the scattering problem in Fig. 7a $[a, a_x]$ and its complex conjugate $[\bar{a}, \bar{a}_x]$ can be also linearly combined to obtain the solution of the scattering problem in Fig. 7b $[a', a'_x]$:

$$[a', a'_x] = -\frac{\bar{c}_r}{\bar{c}_t}[a, a_x] + \frac{1}{\bar{c}_t}[\bar{a}, \bar{a}_x].$$

And the transmission and reflection coefficients for this second scattering problem

can be readily obtained without having to solve another boundary value problem

$$c'_t = c_t \quad \text{and} \quad c'_r = -\bar{c}_r \frac{c_t}{\bar{c}_t}. \quad (38)$$

Note that the magnitude of the transmitted and reflected beams is the same from both sides, even though the defect is not symmetric.

Finally, taking into account the above expressions for the coefficients, the resulting jump conditions at the defect for the slow amplitudes A_1^\pm and A_2^\pm can be written as

$$A_1^+ = c_t A_2^+ + c_r A_1^-, \quad \text{and} \quad A_2^- = c_t A_1^- - \bar{c}_r \frac{c_t}{\bar{c}_t} A_2^+. \quad (39)$$

It is interesting to mention that for the particular case of a symmetric defect,

$$f(x) = f(-x),$$

eq. (31) remains invariant under the change $x \rightarrow -x$, and the two scattering problems in Fig. 7 are just the same problem but observed from opposite directions. The transmission and reflection coefficients of both problems must therefore be the same,

$$c'_t = c_t \quad \text{and} \quad c'_r = c_r,$$

and, using the second relation in (38), we can conclude that for a symmetric defect,

$$|\phi_{c_t} - \phi_{c_r}| = \frac{\pi}{2}, \quad (40)$$

where ϕ_{c_t} and ϕ_{c_r} are the phases of c_t and c_r . Or, in other words, for a symmetric defect the reflection coefficient must be of the form $c_r = i\alpha c_t$, with $\alpha \in \mathbb{R}$.

Results and Discussion

Collecting the results of the previous section, the appropriate envelope equations for the description of the slow scale, weakly nonlinear dynamics of light propagation in a FBG with a narrow defect at $x = 0$ (see Fig. 6) can be finally written as:

$$\begin{aligned}
A_{1T}^+ - A_{1X}^+ &= i\kappa A_1^- + iA_1^+(\sigma|A_1^+|^2 + |A_1^-|^2), \\
A_{1T}^- + A_{1X}^- &= i\kappa A_1^+ + iA_1^-(\sigma|A_1^-|^2 + |A_1^+|^2), \quad \text{for } X < 0, \\
A_{2T}^+ - A_{2X}^+ &= i\kappa A_2^- + iA_2^+(\sigma|A_2^+|^2 + |A_2^-|^2), \\
A_{2T}^- + A_{2X}^- &= i\kappa A_2^+ + iA_2^-(\sigma|A_2^-|^2 + |A_2^+|^2), \quad \text{for } X > 0,
\end{aligned} \tag{41}$$

together with the jump condition (39):

$$A_1^+ = c_t A_2^+ + c_r A_1^-, \quad \text{and} \quad A_2^- = c_t A_1^- - \bar{c}_r \frac{c_t}{\bar{c}_t} A_2^+, \quad \text{at } X = 0,$$

where κ is proportional to the depth of the grating and $\sigma = \frac{1}{2}$. The complex coefficients c_t and c_r are determined by the defect internal shape, and must always verify $|c_t|^2 + |c_r|^2 = 1$.

Computation of the transmission/reflection coefficients

The computation of the reflection and transmission coefficients, c_t and c_r , for a given defect profile $f(x)$ requires to solve the second order ODE (31) together with the the boundary conditions (33) and (34).

In order to do this, we first move the boundary conditions to a finite station $x = \pm x_\infty$, where the defect profile has sufficiently died away, and we compute two linearly independent solutions corresponding to the initial conditions:

$$[a, a_x]_1 = [1, 0] \quad \text{at } x = -x_\infty, \quad \text{and} \quad [a, a_x]_2 = [0, 1] \quad \text{at } x = -x_\infty.$$

The general solution of the problem can be written as a linear combination of these two solutions

$$[a, a_x] = \alpha_1 [a, a_x]_1 + \alpha_2 [a, a_x]_2,$$

where the complex coefficients α_1 and α_2 are given by the following linear system of

equations

$$\begin{bmatrix} ia_1(-x_\infty) + a_{x1}(-x_\infty) & ia_2(-x_\infty) + a_{x2}(-x_\infty) \\ ia_1(x_\infty) - a_{x1}(x_\infty) & ia_2(x_\infty) - a_{x2}(x_\infty) \end{bmatrix} \begin{bmatrix} \alpha_1 \\ \alpha_2 \end{bmatrix} = \begin{bmatrix} 2ie^{-ix_\infty} \\ 0 \end{bmatrix},$$

which results from the application of the boundary conditions (33) and (34). Once the solution $[a, a_x]$ is computed, the reflection and transmission coefficients are readily obtained from eqs. (35) and (36):

$$\begin{aligned} c_r &= (ia(-x_\infty) - a_x(-x_\infty))e^{-ix_\infty}/2i, \\ c_t &= (ia(x_\infty) + a_x(x_\infty))e^{-ix_\infty}/2i. \end{aligned}$$

We have computed the coefficients for the following three representative families of localized defects

$$\begin{aligned} f(x) &= De^{-x^2} && \text{with } D \in [0, 1], \\ f(x) &= De^{-x^2} && \text{with } D \in [-0.85, 0], \\ f(x) &= -D(x + \tfrac{1}{3})e^{-x^2} && \text{with } D \in [0, 1]. \end{aligned}$$

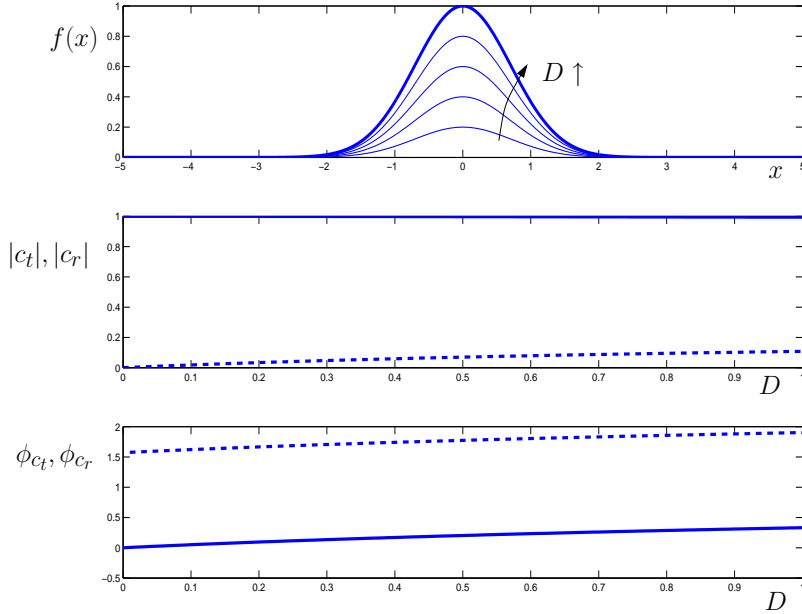


Figure 8: Top: defect profile $f(x) = De^{-x^2}$, with $D \in [0, 1]$. Middle: modulus of the transmission and reflection coefficients. Bottom: phases of the transmission and reflection coefficients.

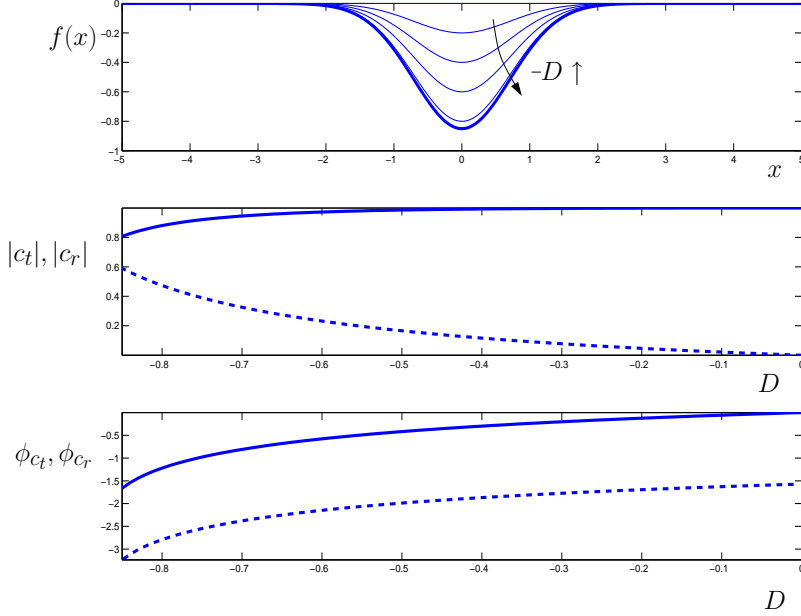


Figure 9: Top: defect profile $f(x) = De^{-x^2}$, with $D \in [-0.85, 0]$. Middle: modulus of the transmission and reflection coefficients. Bottom: phases of the transmission and reflection coefficients.

The first one is symmetric and positive, the second is also symmetric but negative, and the last one is not symmetric and changes sign (see the top plots in Figs. 8, 9 and 10, respectively). The remaining parameters of problem (31) are taken to be

$$n_o^2 = 2, \quad \text{and} \quad \omega_p^2 = 4,$$

and ω^2 is given by eq. (21) using the negative sign, see Fig. 5. The numerical integrations have been performed in MATLAB using a 4th order Runge-Kutta scheme with error below 10^{-6} . The boundary conditions are applied at the finite stations $\pm x_\infty$ with $x_\infty = 6$, and we have checked that increasing x_∞ produces changes in the coefficients that are way below the selected tolerance of 10^{-6} .

The modulus and phases of the resulting transmission and reflection coefficients are plotted in Figs. 8, 9 and 10. It is interesting to mention that for the symmetric positive defect (Fig. 8) the transmission coefficient, c_t , is only slightly reduced when the amplitude of the defect is increased. In other words, the defect remains almost

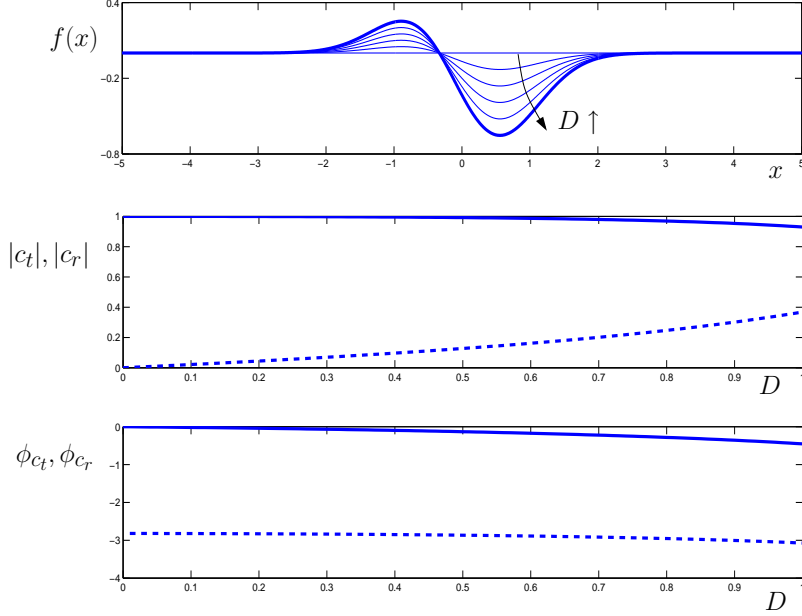


Figure 10: Top: defect profile $f(x) = -D(x + 1/3)e^{-x^2}$, with $D \in [0, 1]$. Middle: modulus of the transmission and reflection coefficients. Bottom: phases of the transmission and reflection coefficients.

transparent as the amplitude of the defect becomes more positive. On the other hand, when the defect is negative, c_t decreases much faster with the amplitude of the defect, that is, the defect is much more opaque than in the positive case; for a negative amplitude $D = -0.85$, $c_t \approx .80$ (see Fig. 9), while for a similar positive amplitude $D = 0.85$, $c_t \approx .995$ (see Fig. 8). This is in perfect agreement with the results plotted in Fig. 2, which showed a much higher sensibility of the refractive index for negative values of the amplitude of the defect $f(x)$. From the bottom plots of Figs. 8 and 9 it can be appreciated that the difference in phase between c_t and c_r is always $\frac{\pi}{2}$, as it is expected for a symmetric defect (see eq. (40)). For the third case, when the defect has both positive and negative parts, the situation is somehow in between the previous two: c_t decays slower than in the negative case, but much faster than in the positive case since the negative part of the defect has higher amplitude than the positive one, see Fig. 10. Note also that in this non-symmetric defect case the difference in phase between c_t and c_r does not remain fixed to $\frac{\pi}{2}$.

Nonlinear defect modes

Defect modes (DM) are standing light pulses that remain localized around the defect. They correspond to permanent in time, light intensity distributions that are zero everywhere except in the vicinity of the defect, see Fig. 11. In this section we construct this type of solutions of the complete problem (41) by joining together two parts of a Gap Soliton.

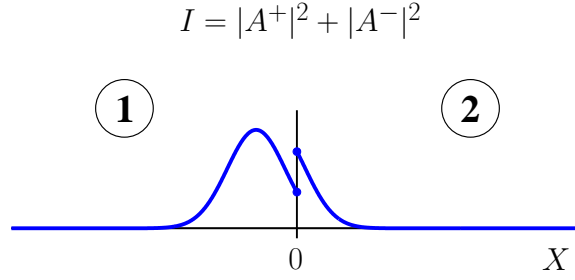


Figure 11: Light intensity distribution of a DM localized at a defect at $X = 0$.

The Gap Solitons (GS) are a well known family of exact solitary wave solutions of the NLCME (29)-(30) that propagate without distortion at any velocity c in the range $|c| < 1$, that is, from 0 to the speed of light of the fiber without grating (see, e.g., [27, 23, 28, 29, 15]). For the particular case of zero propagation velocity, $c = 0$, the standing GS can be written in the form:

$$A_{GS}^+(X, T) = -\sqrt{\kappa}H(X) e^{-i\kappa\gamma T} \quad (42)$$

$$A_{GS}^-(X, T) = \sqrt{\kappa}\bar{H}(X) e^{-i\kappa\gamma T} \quad (43)$$

where

$$\gamma = \cos \theta, \quad \text{with } 0 < \theta < \pi, \quad (44)$$

and the function H is given by

$$H(X) = \frac{\sin \theta}{\sqrt{1 + \sigma} \cosh[X \sin \theta + i\theta/2]}. \quad (45)$$

The standing GS are pulse solutions with steady modulus and temporal frequency

$\kappa\gamma$. The complex function H that gives the profile of the standing GS verifies

$$H(X) = \bar{H}(-X). \quad (46)$$

It has maximum modulus at $X = 0$ and then decays to zero monotonically and exponentially fast as $X \rightarrow \pm\infty$. In Fig 12 we plot the profiles of the standing GS, which, for fixed κ and σ , depend only on the parameter θ .

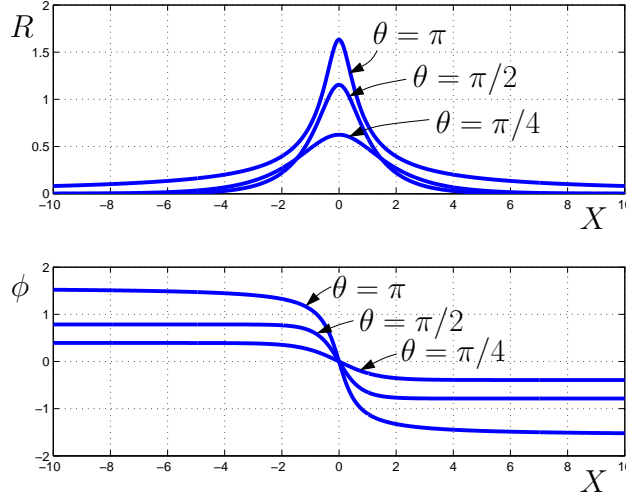


Figure 12: Standing GS profiles for $\theta = \pi/4, \pi/2$, and π . $H(X) = R(X)e^{i\phi(X)}$, modulus $R(X)$ (top plot) and phase $\phi(X)$ (bottom plot).

As sketched in Fig 13, we can join two pieces of a standing GS to form a DM. The GS are exact solutions of the NLCME and therefore the resulting DM verifies the differential equations for A_1^\pm and A_2^\pm in the system (41). It must verify also the jump conditions (39):

$$A_1^+ = c_t(A_2^+ + \alpha A_1^-), \quad \text{and} \quad A_2^- = c_t(A_1^- - \bar{\alpha} A_2^+), \quad (47)$$

with $\alpha = c_r/c_t$. The values of A_1^\pm and A_2^\pm are given by the expression of the standing GS (42)-(43) at $X = X_1$ and $X = X_2$ (see Fig 13), and once inserted into the jump

conditions produce:

$$\begin{aligned} -R_1 e^{i\phi_1} &= c_t (-R_2 e^{i\phi_2} + \alpha R_1 e^{-i\phi_1}), \\ R_2 e^{-i\phi_2} &= c_t (R_1 e^{-i\phi_1} + \bar{\alpha} R_2 e^{i\phi_2}), \end{aligned}$$

where $H(X_1) = R_1 e^{i\phi_1}$ and $H(X_2) = R_2 e^{i\phi_2}$. From the equations above we can easily obtain the transmission and reflection coefficients

$$c_t = \cos \psi \frac{2R_1 R_2}{R_1^2 + R_2^2} e^{i((\phi_1 - \phi_2) - \psi)}, \quad (48)$$

$$c_r = \left(\cos \psi \frac{R_2^2 - R_1^2}{R_1^2 + R_2^2} - i \sin \psi \right) e^{i(2\phi_1 - \psi)}, \quad (49)$$

which depend on the limit points of the GS pieces, X_1 and X_2 , and on the free parameter $-\frac{\pi}{2} < \psi < \frac{\pi}{2}$, and verify the conservation condition (37): $|c_t|^2 + |c_r|^2 = 1$.

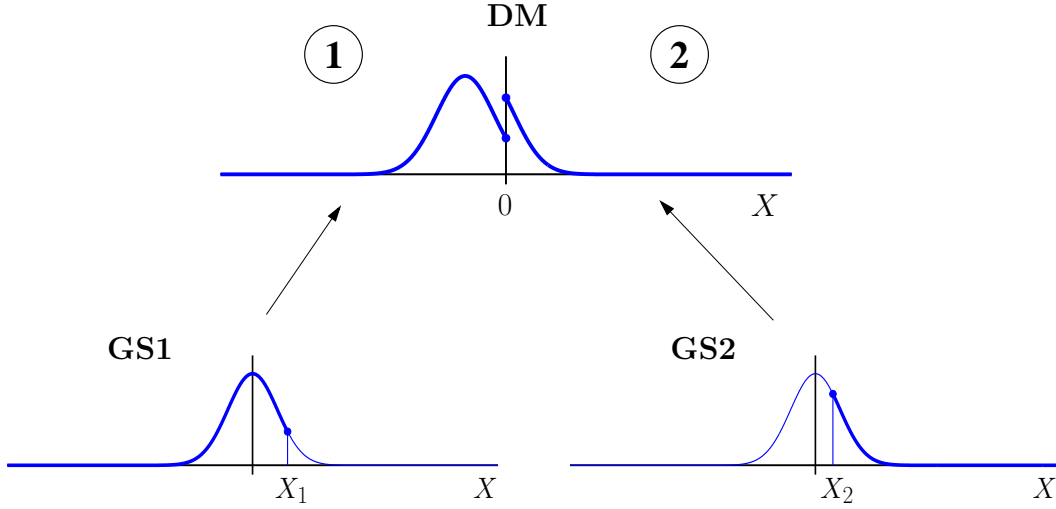


Figure 13: Construction of a DM joining two pieces of a standing GS.

Generally speaking, one can use the expressions above to obtain, for given values of c_t and c_r , the corresponding DM, which are defined by the parameters X_1 , X_2 and ψ . Note that, because of the conservation condition (37), prescribing the values of the complex numbers c_t and c_r corresponds to imposing only three real conditions and, therefore, we have the appropriate number of equations for the determination

of the three real parameters of the DM.

Instead of analyzing the DM in the general form given by (48)-(49), we will restrict our attention to two particular families of DM that share the property $R_1 = R_2$ (i.e. no jump of the modulus across the defect). The transmission and reflection coefficients for these two families take the simplified form:

- DM1: $X_1 = X_2$, $R_1 = R_2$, and $\phi_1 = \phi_2$,

$$c_t = \cos \psi e^{-i\psi}, \quad (50)$$

$$c_r = -i \sin \psi e^{i(2\phi_1 - \psi)}. \quad (51)$$

- DM2: $X_1 = -X_2$, $R_1 = R_2$, and $\phi_1 = -\phi_2$,

$$c_t = \cos \psi e^{i(2\phi_1 - \psi)}, \quad (52)$$

$$c_r = -i \sin \psi e^{i(2\phi_1 - \psi)}. \quad (53)$$

The expressions above depend only on two parameters, $-\infty < X_1 < \infty$ and $-\frac{\pi}{2} < \psi < \frac{\pi}{2}$, and they span all possible cases between total transmission $c_r = 0$ and total reflection $c_t = 0$, see Fig 14.

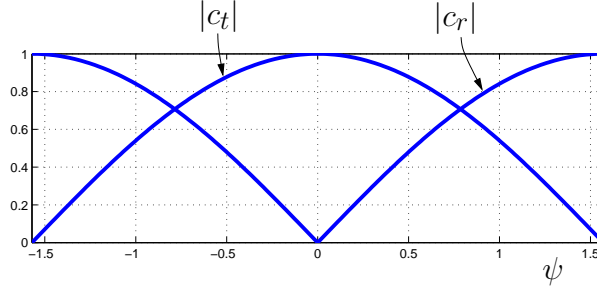


Figure 14: Transmission, c_t , and reflection, c_r , coefficient size for the defect mode families DM1 and DM2.

The profiles of the defect modes in family DM1 are sketched in Fig 15. They correspond to non-symmetric defects and, for $\psi = 0$, they reproduce the trivial situation of no defect at all ($c_t = 1$ and $c_r = 0$). If we apply a spatial reflection symmetry to the complete system (41): $X \rightarrow -X$ and $A_1^\pm \leftrightarrow A_2^\mp$, then the equations

remain invariant, c_t does not change either, but c_r becomes $c'_r = -\bar{c}_r \frac{c_t}{c_t}$. For the DM1 family this implies that the problem for the DM for a given X_1 is the same as for $-X_1$ and, therefore, it is enough to study the case $X_1 \geq 0$.

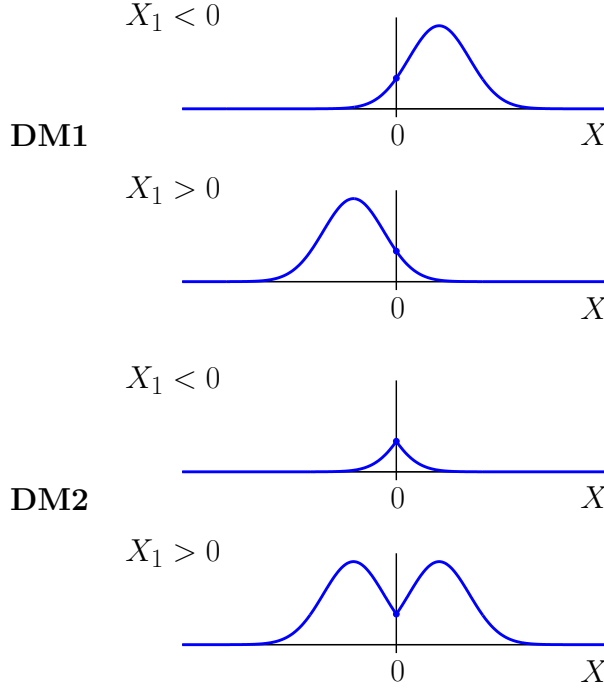


Figure 15: Sketch of the profiles of the defect modes in families DM1 and DM2.

The second family DM2 corresponds to symmetric defects, i.e., $c_r = -\bar{c}_r \frac{c_t}{c_t}$, and the reflection symmetry does not provide now any reduction of the parameter space. This is precisely the family of symmetric DM derived in [17] using a localized defect formulation based in the addition of Dirac delta functions to the standard NLCME. In [17] the dynamics of the defect modes was analyzed including only a local disruption of the Bragg grating reflection and without local perturbation of the refractive index. This situation corresponds in our formulation to the particular case of $\psi = 2\phi_1$, which gives real c_t and purely imaginary c_r .

Defect mode stability

We analyze the stability properties of the defect modes obtained in the previous section. We fix $\theta = \pi/4$ so the standing GS used to generate the DM is stable (see [28, 29]), and we study the stability of the complete families DM1 and DM2 for $-\infty < X_1 < \infty$ and $-\frac{\pi}{2} < \psi < \frac{\pi}{2}$.

For each value of X_1 and ψ we compute the corresponding coefficients c_t and c_r , and the associated DM. We then run a numerical simulation of equations (41) using as initial condition the DM with a small superimposed random perturbation. If the DM persists in time we consider it stable, and unstable if the system evolves away from it. The details of the numerical method used to integrate equations (41) can be found in the final section of this chapter, and the particular values of the numerical parameters are as follows: spatial domain $X \in [-20, 20]$, final integration time $T = 200$, size of the perturbation added 10^{-3} , time step $\Delta T = .01$, and grid spacing $\Delta X = .01$.

The stability results for the family DM1 are presented in Fig 16, where the red dots in the plane $X_1 - \psi$ indicate the unstable DM. The DM1 family is $X_1 \leftrightarrow -X_1$ symmetric and so is the resulting instability region (up to the approximation of the method). Note also that, as $|X_1|$ grows, the defect is located further in the tail of the GS and becomes less relevant, and thus, for large $|X_1|$, we recover the stable dynamics of the GS without defect. A typical stable DM of this family is represented in the sub-figure 1. In the top plot we show the initial ($T = 0$) and final ($T = 200$) profiles of the solution, which are basically indistinguishable. The bottom plot of the sub-figure shows a log plot of the temporal evolution of the quantity:

$$\left\| \frac{\partial |A|}{\partial T} \right\|$$

for the four amplitudes A_1^\pm and A_2^\pm . The modulus of the DM is steady and therefore this magnitude indicates easily the departure from the DM solution. For this stable case this magnitudes decay from the initial perturbation, and remain always very small $\sim 10^{-6}$. Two regions of instability can be appreciated in Fig 16. In sub-figure 2 we plot a solution inside the instability region near $\psi = \pi/2$. The regular oscillations in the bottom plot indicate that it corresponds to a Hopf destabilization with a clear temporal frequency of about $T \sim 8$. The solution starts to oscillate

in time and it takes about 150 time units to clearly depart from the original DM. Sub-figure 3 corresponds to a typical solution inside the instability region located at $\psi < 0$. Note that this instability does not have a clear frequency and that it exhibits has a much higher growth rate: it takes only 40 time units to completely destroy the original DM.

Fig 17 shows the stability properties of family DM2. The DM in this family correspond to $X \leftrightarrow -X$ symmetric defects, and there are stable DM with a single maximum (for $X_1 < 0$, see sub-figure 1) and also with two maxima (for $X_1 > 0$, see sub-figure 3). In this case the DM become unstable as X_1 is increased (i.e., as the distance between the maxima grows) and, for $X_1 = 2.5$, they are all unstable, independently of the value of ψ . If $|X_1|$ is further increased, then the defect moves to the tail of the GS and we recover again the stability of the GS, even in the two maxima case $X_1 > 0$. There appears to be again two unstable regions: one large covering all ranges of ψ , and a small one near $\psi = \pi/2$. In sub-figure 2 a typical solution of the large unstable area is depicted; the growth rate of the instability is quite large and the original DM is completely destroyed for $T = 70$. A solution from the other instability region is represented in sub-figure 4. As it happened for the DM1 family, the instability onset is now oscillatory and the growth rate is clearly much smaller.

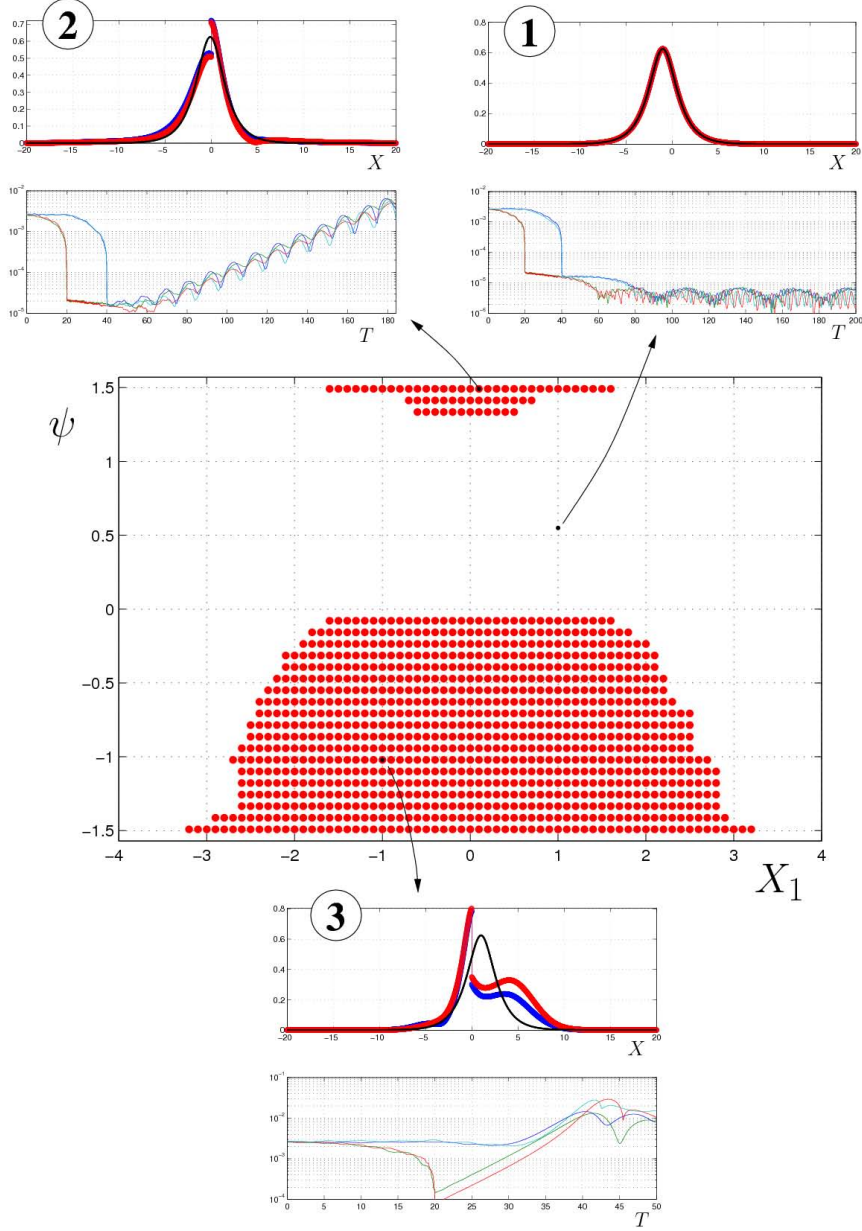


Figure 16: Stability of the DM1 family as a function of X_1 and ψ . Red dots indicate instability. The solution is also shown for three representative cases (marked with black dots). Top plots: spatial profiles of $|A^+|$ (blue line) and $|A^-|$ (red line) at the end of the simulation, and the profile of the DM used as initial condition (black line). Bottom plots: temporal evolution of the norms $\|\frac{\partial}{\partial T}|A_{1,2}^\pm|\|$.

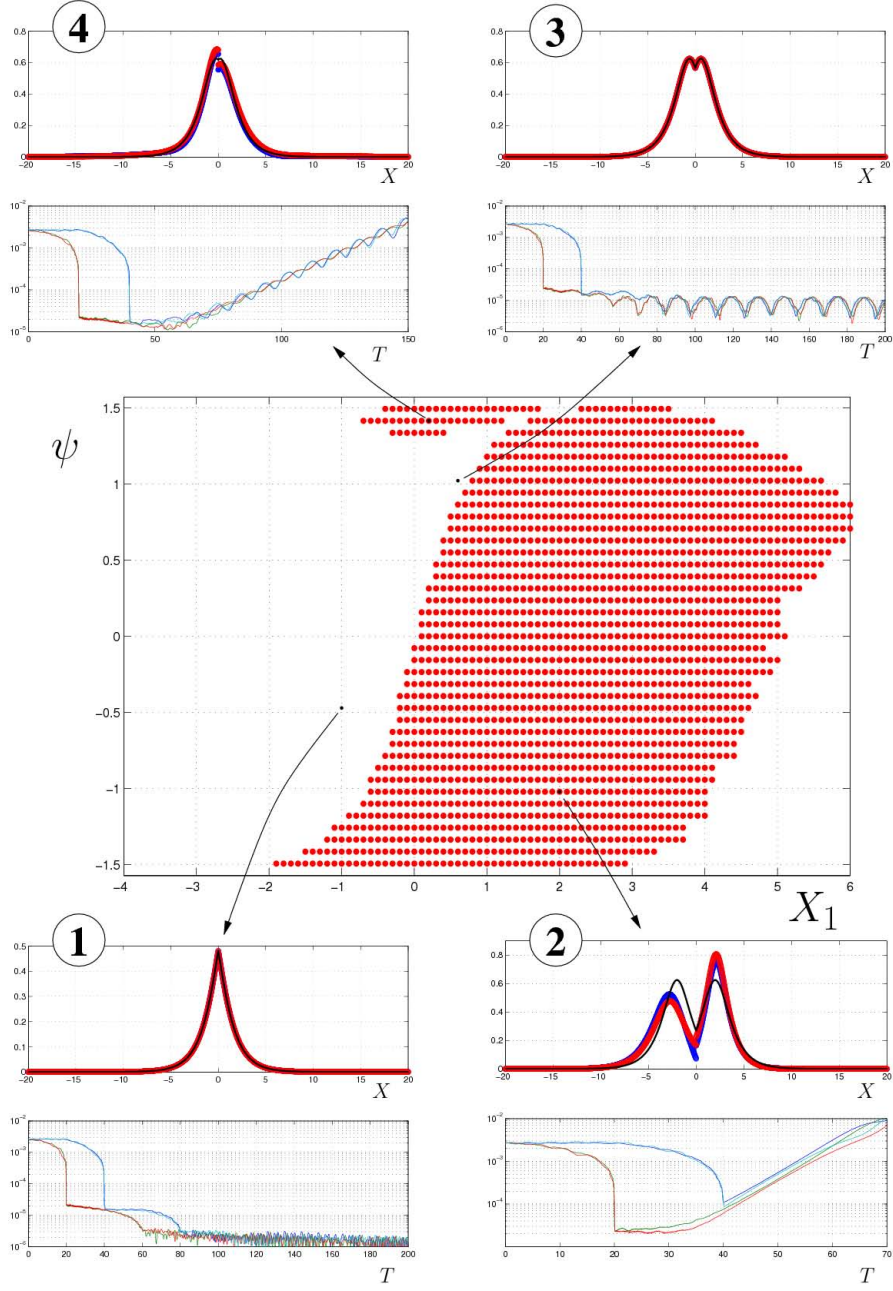


Figure 17: Stability of the DM2 family as a function of X_1 and ψ . Red dots indicate instability. The solution is also shown for four representative cases (marked with black dots). Top plots: spatial profiles of $|A^+|$ (blue line) and $|A^-|$ (red line) at the end of the simulation, and the profile of the DM used as initial condition (black line). Bottom plots: temporal evolution of the norms $\|\frac{\partial}{\partial T} |A_{1,2}^\pm|\|$.

Pulse trapping simulations

In this section we explore the light trapping characteristics of two representative defects from the families DM1 and DM2 analyzed in the previous section. We send a propagating GS and simulate numerically its collision with a defect. The time evolution of the system (41) is computed with the numerical method described in the next section, using a very large spatial domain $[-100, 100]$ and with resolution $\Delta X = .01$ and $\Delta T = .01$.

The initial condition in all simulations is a right moving GS centered at $X = -40$. The moving GS are a well known (see, e.g., [27, 23, 28, 29, 15]) family of propagating pulse like solutions of the NLCME (29)-(30) that can be written in the form

$$\begin{aligned} A_{GS}^+(X, T) &= -\sqrt{\kappa} H(\xi) e^{-y/2 + i\varphi(\xi) - i\kappa\gamma T} \\ A_{GS}^-(X, T) &= \sqrt{\kappa} \bar{H}(\xi) e^{y/2 + i\varphi(\xi) - i\kappa\gamma T} \end{aligned}$$

where $\xi = \kappa(X - cT)$ is a moving spatial coordinate, c is the velocity of the GS

$$c = \tanh y, \quad \text{with } -\infty < y < +\infty,$$

$\kappa\gamma$ is its temporal frequency, with

$$\gamma = \cos \theta / \cosh y = \cos \theta \sqrt{1 - c^2}, \quad \text{with } 0 < \theta < \pi,$$

and the functions H and φ are given by

$$\begin{aligned} \varphi(\xi) &= \frac{2\sigma \sinh(2y) \arctan\{\tan(\theta/2) \tanh[(\cosh y \sin \theta)\xi]\}}{1 + \sigma \cosh 2y} + (\sinh y \cos \theta)\xi, \\ H(\xi) &= \frac{\sin \theta}{\sqrt{1 + \sigma \cosh 2y} \cosh[(\cosh y \sin \theta)\xi + i\theta/2]}. \end{aligned}$$

Note that the moving GS above are a two parameter, $c - \gamma$, family of solutions that, in the particular case of zero propagation velocity $c = 0$, reduce to the standing GS previously used to obtain the DM. In Fig 18 we represent the profile of a moving GS and its domain of existence: $c^2 + \gamma^2 = 1$.

The first set of simulations corresponds to a non-symmetric defect of the DM1

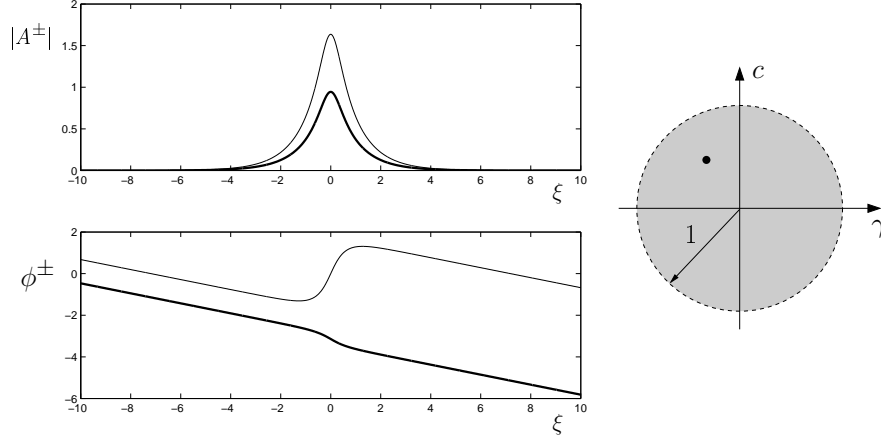


Figure 18: Left: moving Gap Soliton at $t = 0$, $A^+(A^-)$ thick (thin) line, with parameters $\sigma = \frac{1}{2}$, $\kappa = 1$, $c = \frac{1}{2}$ and $\theta = 2$. Right: domain of existence of the GS in the $c - \gamma$ plane (the dot corresponds to the GS shown).

family labeled 1 in Fig. 16. The parameters in system (41) for this case are $\kappa = 1$ and $\sigma = 1/2$, and the transmission and reflection coefficient are given by

$$c_t = 0.7270 - 0.4455i, \quad c_r = -0.4516 - 0.2628i,$$

which correspond to the parameters in eqs. (50)-(51): $\theta = \pi/4$, $X_1 = 1$ and $\psi = 0.5498$. The associated standing nonlinear DM is stable and is represented in sub-figure 1 of Fig 16. The temporal frequency of this DM is $1/\sqrt{2}$ (see eqs. (42), (43) and (44)) so, in order to try to excite it, we send moving GS solitons from the left with the same temporal frequency, $\gamma = 1/\sqrt{2}$, and velocities $c = 0.2, 0.3, 0.4, 0.5, 0.6$. The results are presented in Figs. 19 to 23, where the $X - T$ diagram of the light intensity during the collision of the moving GS with the defect (located at $X = 0$) is represented together with the profiles of the solution at initial and final time. Note that for low velocities $c = 0.2$ and $c = 0.3$ (Figs. 19 and 20) the GS is basically reflected, and for higher velocities $c = 0.4$, $c = 0.5$ and $c = 0.6$ (Figs. 21, 22 and 23) the GS just passes through the defect. In all cases some radiation is shed, but no light intensity remains trapped at the defect. The speed of the pulse coming out of the collision with the defect is negative for $c = 0.3$ (see Fig. 20) and positive for $c = 0.4$ (see Fig. 21), so one can try to adjust c to end up having a standing pulse after the collision. But this kind behavior with GS trapping only for a single value

of c is a non-robust, unstable situation that has not much interest since in a realistic setting we will never be sending the exact GS, and therefore we will always end up with a pulse slowly drifting away from the defect.

In the second set of simulations we analyze a symmetric defect of the DM2 family. To be more precise the one that is labeled 1 in Fig 17, which corresponds to $\kappa = 1$ and $\sigma = 1/2$, transmission and reflection coefficient

$$c_t = 0.5071 + 0.7326i, \quad c_r = -0.3733 - 0.2584i,$$

and parameters $\theta = \pi/4$, $X_1 = -1$ and $\psi = -0.4712$ in eqs. (52)-(53). The associated DM is stable (see sub-figure 1 of Fig 17) and has again temporal frequency $1/\sqrt{2}$. The initial condition in all simulations is again a left going GS, centered at $X = -40$, with frequency $\gamma = 1/\sqrt{2}$, and velocities $c = 0.2, 0.3, 0.4, 0.5, 0.6$. The results of the collisions with the defect are presented in Figs. 24 to 28. For small velocity $c = 0.2$ (see Fig. 24) a large part of the intensity of the incoming GS is trapped by the defect, that ends up exhibiting a pulsating localized defect mode. As the velocity of the GS is increased, the intensity of the trapped pulse is reduced and its oscillatory character ceases at $c = 0.4$ (see Figs. 26). Also, from $c = 0.4$ and above an outgoing pulse from the collision with the defect can be clearly identified (see Figs. 26, 27 and 28), which looks like a GS different from the initially sent one. The situation is now for this symmetric defect completely different: for all GS velocities there is always trapping of light intensity by the defect, in what appears to be a quite robust behavior.

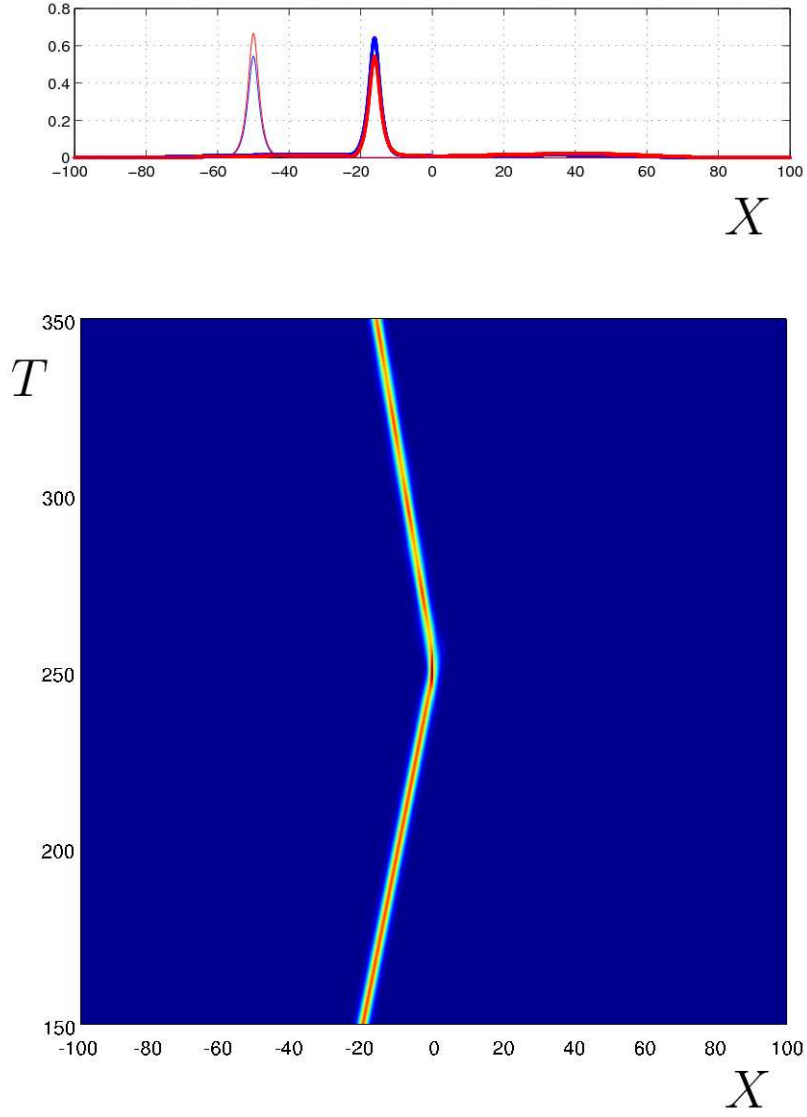


Figure 19: DM1 defect interaction with a GS of speed $c = 0.2$ sent from the left. Bottom: $X - T$ diagram of the light intensity, $I = \sqrt{|A^+|^2 + |A^-|^2}$, during collision. Top: profiles of $|A^+|$ in blue and $|A^-|$ in red at $T = 0$ (thin lines) and $T = 350$ (thick lines).

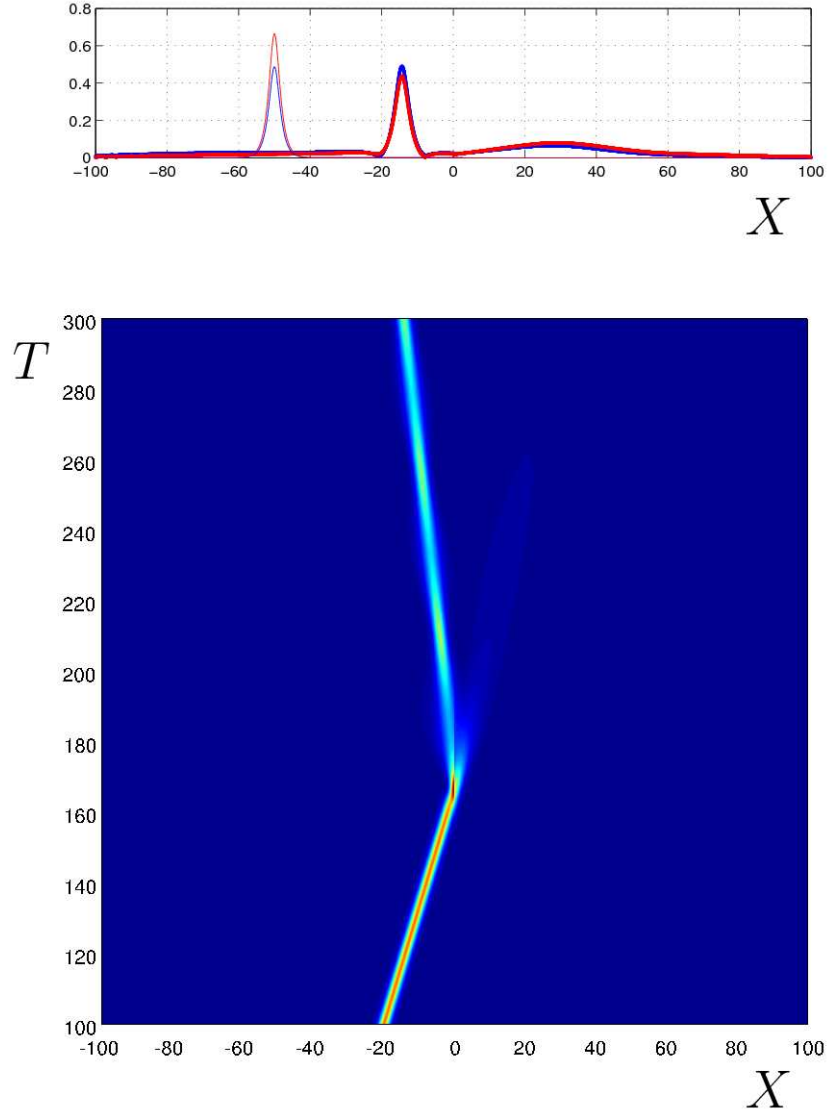


Figure 20: DM1 defect interaction with a GS of speed $c = 0.3$ sent from the left. Bottom: $X - T$ diagram of the light intensity, $I = \sqrt{|A^+|^2 + |A^-|^2}$, during collision. Top: profiles of $|A^+|$ in blue and $|A^-|$ in red at $T = 0$ (thin lines) and $T = 300$ (thick lines).

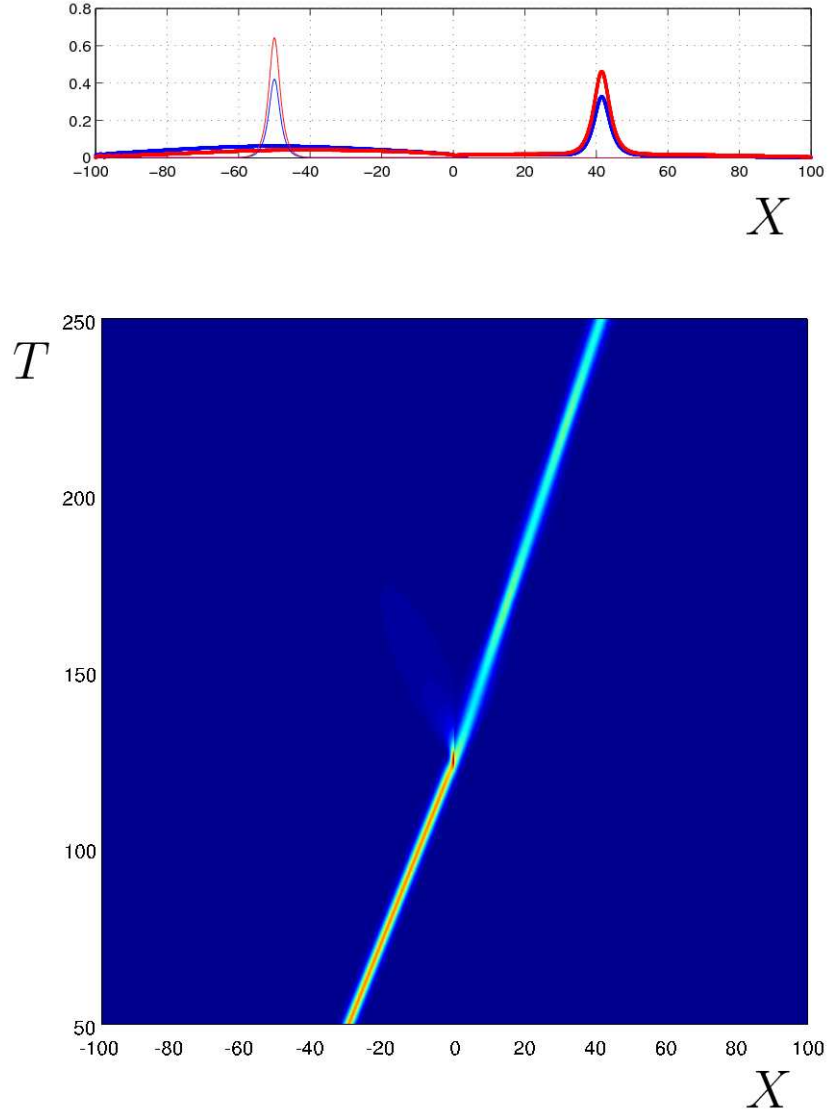


Figure 21: DM1 defect interaction with a GS of speed $c = 0.4$ sent from the left. Bottom: $X - T$ diagram of the light intensity, $I = \sqrt{|A^+|^2 + |A^-|^2}$, during collision. Top: profiles of $|A^+|$ in blue and $|A^-|$ in red at $T = 0$ (thin lines) and $T = 250$ (thick lines).

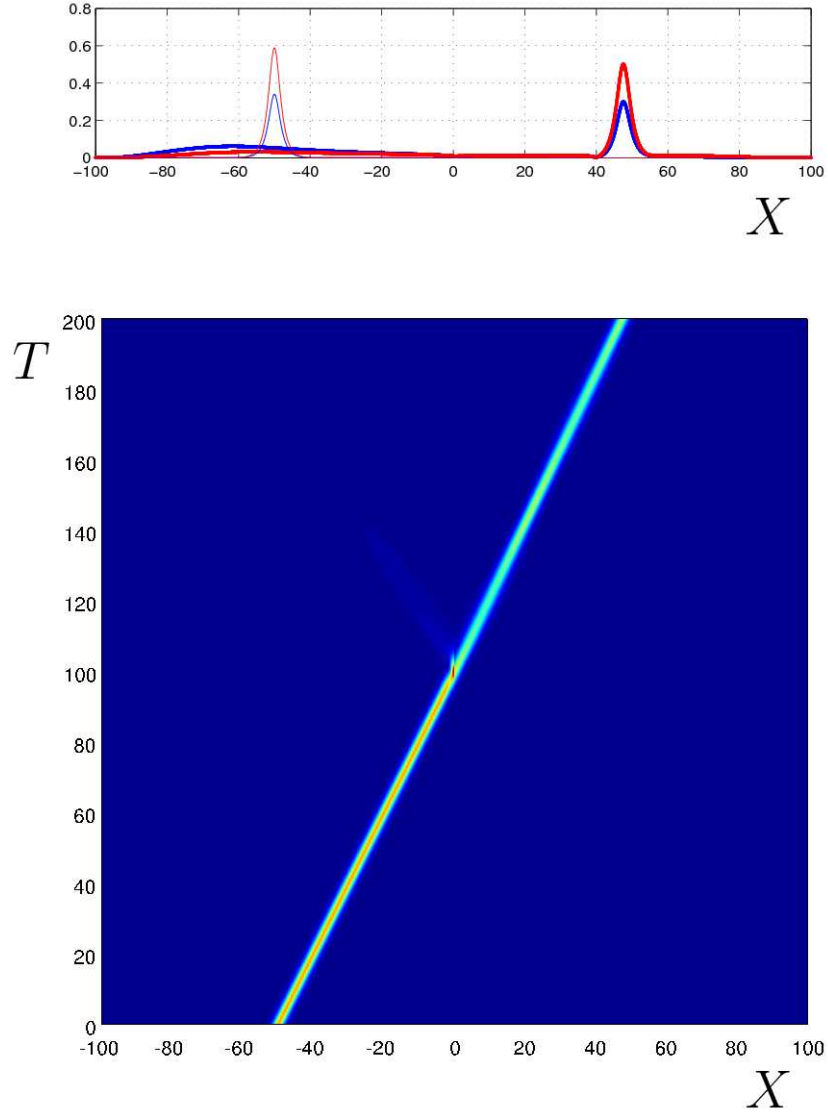


Figure 22: DM1 defect interaction with a GS of speed $c = 0.5$ sent from the left. Bottom: $X - T$ diagram of the light intensity, $I = \sqrt{|A^+|^2 + |A^-|^2}$, during collision. Top: profiles of $|A^+|$ in blue and $|A^-|$ in red at $T = 0$ (thin lines) and $T = 200$ (thick lines).

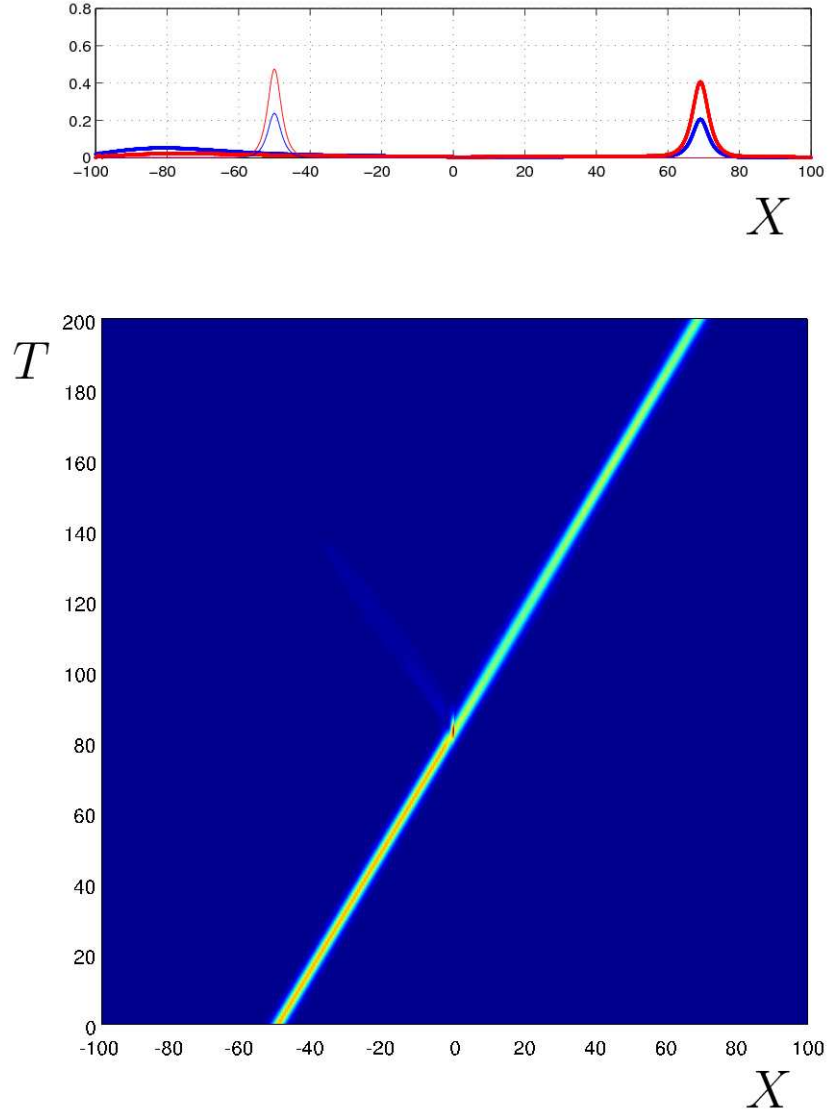


Figure 23: DM1 defect interaction with a GS of speed $c = 0.6$ sent from the left. Bottom: $X - T$ diagram of the light intensity, $I = \sqrt{|A^+|^2 + |A^-|^2}$, during collision. Top: profiles of $|A^+|$ in blue and $|A^-|$ in red at $T = 0$ (thin lines) and $T = 200$ (thick lines).

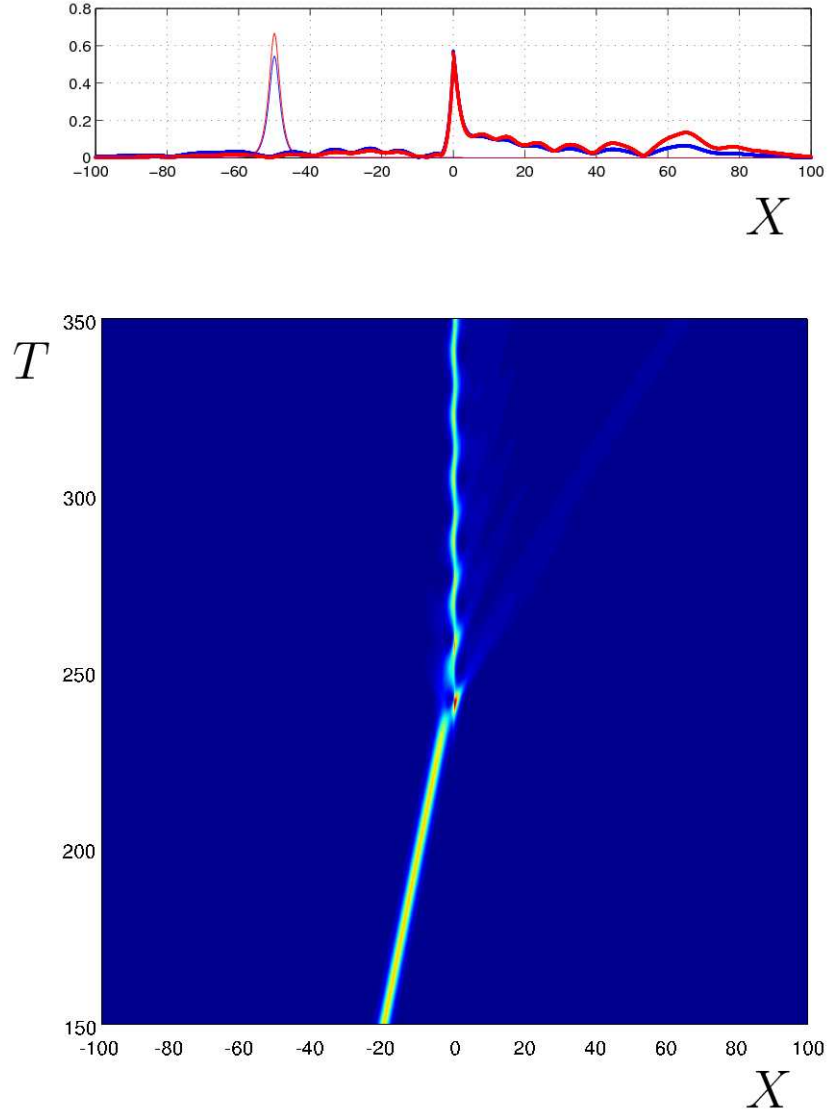


Figure 24: DM2 defect interaction with a GS of speed $c = 0.2$ sent from the left. Bottom: $X - T$ diagram of the light intensity, $I = \sqrt{|A^+|^2 + |A^-|^2}$, during collision. Top: profiles of $|A^+|$ in blue and $|A^-|$ in red at $T = 0$ (thin lines) and $T = 350$ (thick lines).

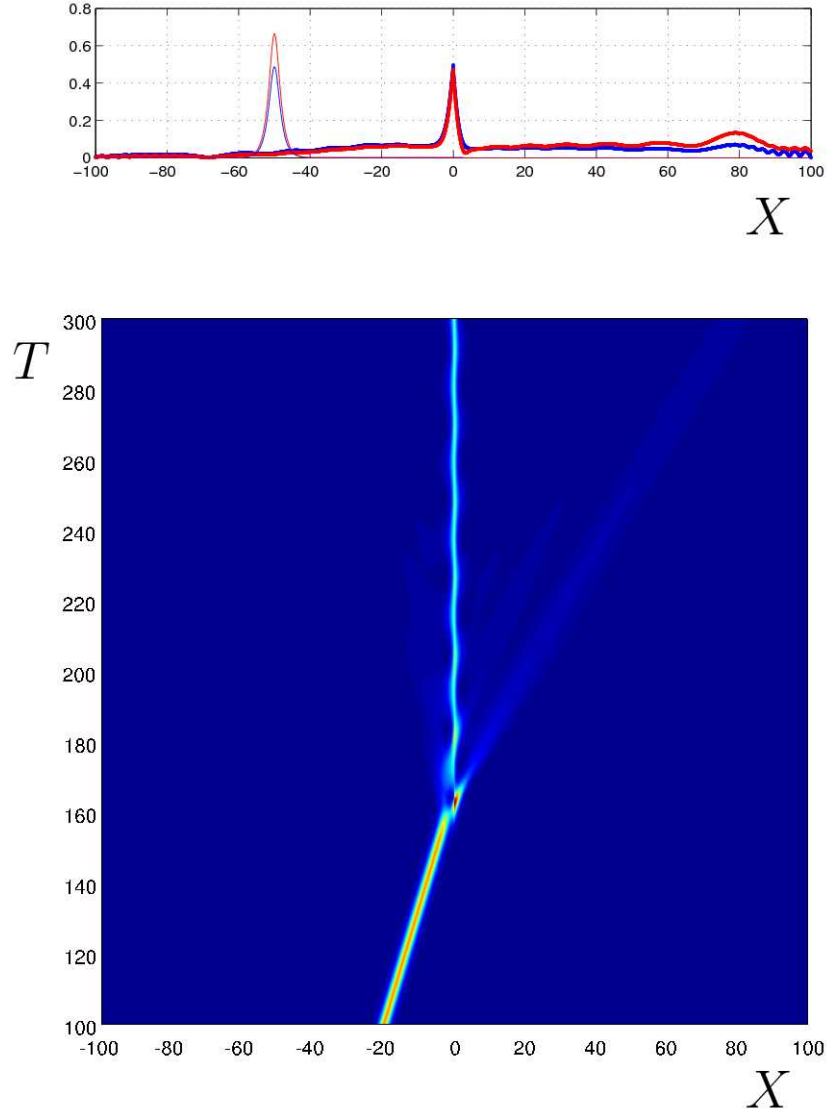


Figure 25: DM2 defect interaction with a GS of speed $c = 0.3$ sent from the left. Bottom: $X - T$ diagram of the light intensity, $I = \sqrt{|A^+|^2 + |A^-|^2}$, during collision. Top: profiles of $|A^+|$ in blue and $|A^-|$ in red at $T = 0$ (thin lines) and $T = 300$ (thick lines).

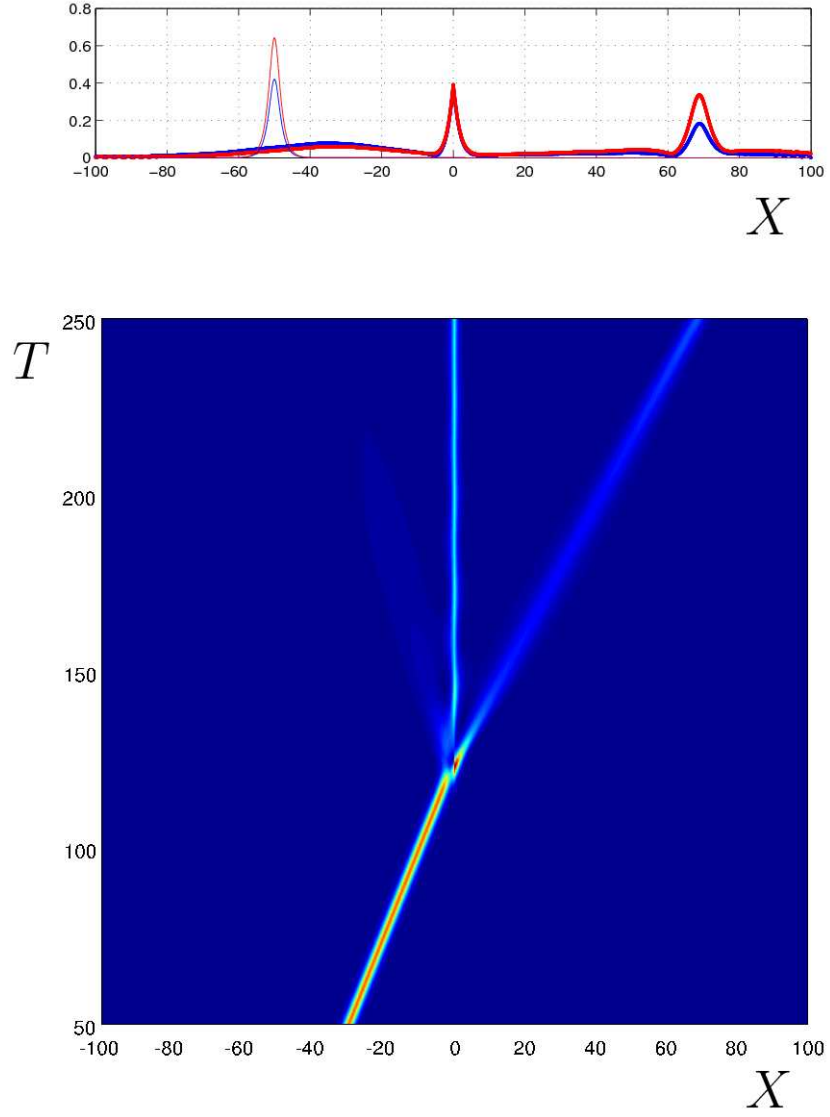


Figure 26: DM2 defect interaction with a GS of speed $c = 0.4$ sent from the left. Bottom: $X - T$ diagram of the light intensity, $I = \sqrt{|A^+|^2 + |A^-|^2}$, during collision. Top: profiles of $|A^+|$ in blue and $|A^-|$ in red at $T = 0$ (thin lines) and $T = 250$ (thick lines).

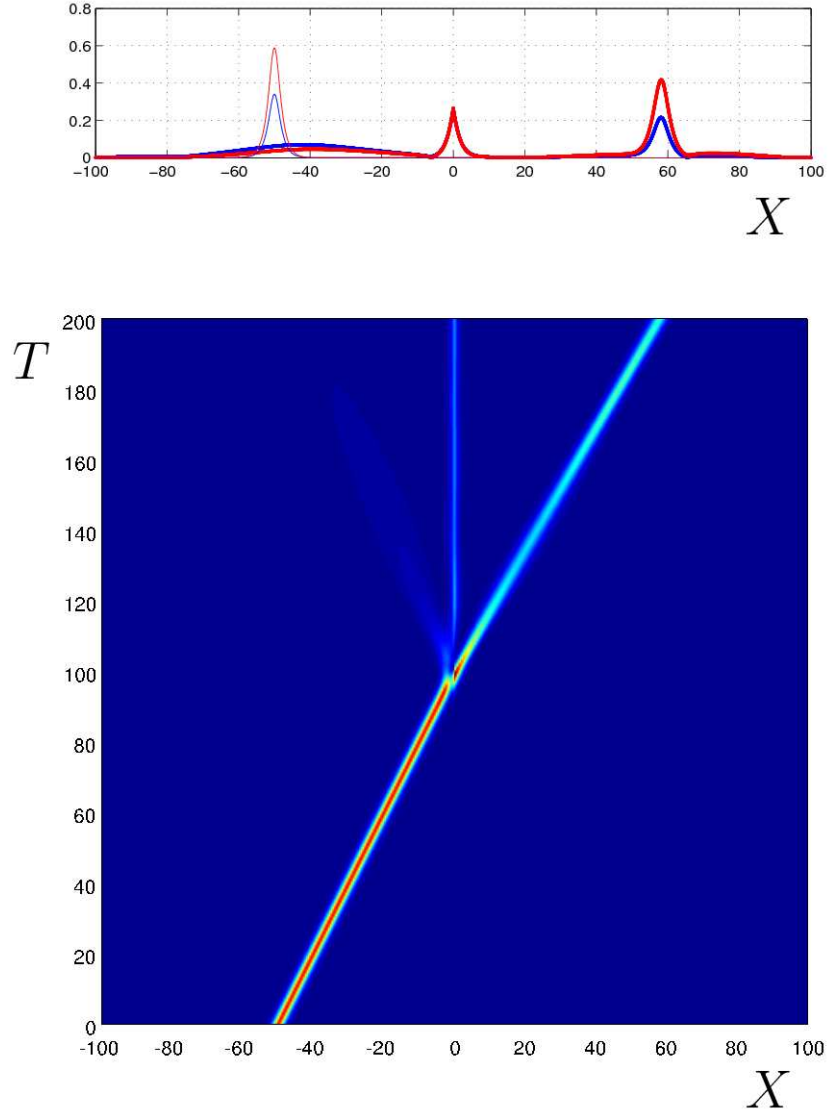


Figure 27: DM2 defect interaction with a GS of speed $c = 0.5$ sent from the left. Bottom: $X - T$ diagram of the light intensity, $I = \sqrt{|A^+|^2 + |A^-|^2}$, during collision. Top: profiles of $|A^+|$ in blue and $|A^-|$ in red at $T = 0$ (thin lines) and $T = 200$ (thick lines).

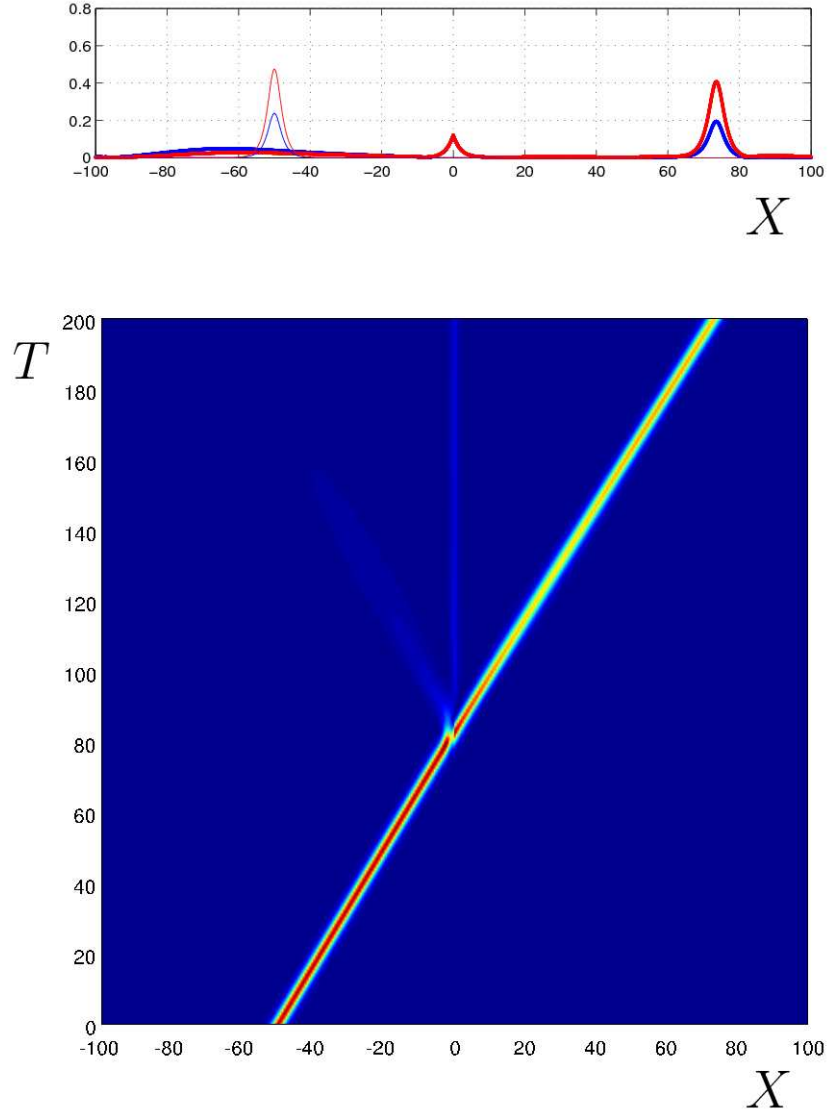


Figure 28: DM2 defect interaction with a GS of speed $c = 0.6$ sent from the left. Bottom: $X - T$ diagram of the light intensity, $I = \sqrt{|A^+|^2 + |A^-|^2}$, during collision. Top: profiles of $|A^+|$ in blue and $|A^-|$ in red at $T = 0$ (thin lines) and $T = 200$ (thick lines).

Numerical simulation of light propagation in a FBG with a defect

To simulate the dynamics of light propagation in an FBG with a sharp defect we have to numerically integrate the problem (41) in a finite domain $[-L, L]$:

$$\begin{aligned} A_{1T}^+ - A_{1X}^+ &= i\kappa A_1^- + iA_1^+(\sigma|A_1^+|^2 + |A_1^-|^2), \\ A_{1T}^- + A_{1X}^- &= i\kappa A_1^+ + iA_1^-(\sigma|A_1^-|^2 + |A_1^+|^2), \quad \text{for } X < 0, \\ A_{2T}^+ - A_{2X}^+ &= i\kappa A_2^- + iA_2^+(\sigma|A_2^+|^2 + |A_2^-|^2), \\ A_{2T}^- + A_{2X}^- &= i\kappa A_2^+ + iA_2^-(\sigma|A_2^-|^2 + |A_2^+|^2), \quad \text{for } X > 0, \end{aligned}$$

together with the jump conditions (39):

$$A_1^+ = c_t A_2^+ + c_r A_1^-, \quad \text{and} \quad A_2^- = c_t A_1^- - \bar{c}_r \frac{c_t}{\bar{c}_t} A_2^+, \quad \text{at } X = 0,$$

and the appropriate boundary conditions at $X = \pm L$:

$$A_1^-(-L, T) = F_1(T) \quad \text{at } X = -L, \quad \text{and} \quad A_2^+ = F_2(T), \quad \text{at } X = L.$$

We use a uniform spatial grid with spacing $\Delta X = L/N$, and a second order approximation for the amplitudes and its spatial derivatives at the mid points of the grid (see Fig 29). The resulting discretized ODEs are given by

$$\begin{aligned} \frac{d}{dT} \left(\frac{A_{i+1}^+ + A_i^+}{2} \right) &= \left(\frac{A_{i+1}^+ - A_i^+}{\Delta X} \right) + i\kappa \left(\frac{A_{i+1}^- - A_i^-}{2} \right) + \frac{NL_{i+1}^+ + NL_i^+}{2} + \mathcal{O}(\Delta X^2), \\ \frac{d}{dT} \left(\frac{A_{i+1}^- + A_i^-}{2} \right) &= - \left(\frac{A_{i+1}^- - A_i^-}{\Delta X} \right) + i\kappa \left(\frac{A_{i+1}^+ - A_i^+}{2} \right) + \frac{NL_{i+1}^- + NL_i^-}{2} + \mathcal{O}(\Delta X^2), \end{aligned}$$

where the terms NL^\pm account for the nonlinear terms of the equations for A^\pm , respectively. We can rewrite the equations above in matrix form as

$$\begin{aligned} \begin{bmatrix} 1 & 0 & 1 & 0 \\ 0 & 1 & 0 & 1 \end{bmatrix} \frac{d}{dT} \begin{bmatrix} A_i^+ \\ A_i^- \\ A_{i+1}^+ \\ A_{i+1}^- \end{bmatrix} &= \left(\frac{2}{\Delta X} \begin{bmatrix} -1 & 0 & 1 & 0 \\ 0 & 1 & 0 & -1 \end{bmatrix} + i\kappa \begin{bmatrix} 1 & 0 & 1 & 0 \\ 0 & 1 & 0 & 1 \end{bmatrix} \right) \begin{bmatrix} A_i^+ \\ A_i^- \\ A_{i+1}^+ \\ A_{i+1}^- \end{bmatrix} \\ &+ \begin{bmatrix} 1 & 0 & 1 & 0 \\ 0 & 1 & 0 & 1 \end{bmatrix} \begin{bmatrix} NL_i^+ \\ NL_i^- \\ NL_{i+1}^+ \\ NL_{i+1}^- \end{bmatrix}. \end{aligned}$$

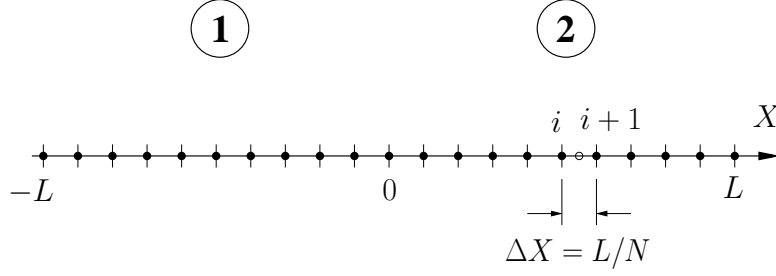


Figure 29: Discretization of the spatial domain $[-L, L]$.

We apply these equations at each mid point in regions 1 and 2 (see Fig 29) and obtain $4N$ equations for the $4(N+1)$ amplitudes at the grid points, which we store in the vector

$$A = [A_{1,1}^+, A_{1,1}^-, \dots, A_{1,N+1}^+, A_{1,N+1}^-, A_{2,1}^+, A_{2,1}^-, \dots, A_{2,N+1}^+, A_{2,N+1}^-]^T.$$

The remaining 4 equations are obtained from the jump conditions (39),

$$\begin{bmatrix} 1 & -c_r & -c_t & 0 \\ 0 & -c_t & \bar{c}_r \frac{c_t}{c_t} & 1 \end{bmatrix} \begin{bmatrix} A_{1,N+1}^+ \\ A_{1,N+1}^- \\ A_{2,1}^+ \\ A_{2,1}^- \end{bmatrix} = \begin{bmatrix} 0 \\ 0 \end{bmatrix},$$

and the boundary conditions

$$A_{1,1}^- = F_1(T) \quad , \text{and} \quad A_{2,N+1}^+ = F_2(T).$$

The complete discretized problem can be casted as a system of $4(N+1)$ differential algebraic equations of the form:

$$M_T \frac{dA}{dT} = M_L A + M_{NL} NL + M_{BC} A - BC, \quad (54)$$

where the $4(N+1) \times 4(N+1)$ matrices M_T , M_L , M_{BC} and M_{NL} do not depend on T and are highly sparse, and the vectors NL and BC are $4(N+1)$ long and contain the nonlinear terms,

$$NL = [NL_{1,1}^+, NL_{1,1}^-, \dots, NL_{1,N+1}^+, NL_{1,N+1}^-, NL_{2,1}^+, NL_{2,1}^-, \dots, NL_{2,N+1}^+, NL_{2,N+1}^-]^T,$$

and input from the boundary conditions,

$$BC = [F_1(T), 0, \dots, 0, F_2(T)]^T.$$

The algebraic equations come from the jump and the boundary conditions, and are placed at the rows 1, $2(N+1)$, $2(N+1)+1$, and $4(N+1)$ of the system. The matrix M_{BC} is different from zero only in these rows, where the rest of the the matrices M_T , M_L , and M_{NL} do not contribute.

Finally, the time integration of (54) is performed using a second order Runge-Kutta scheme. In order to ensure the stability of the resulting scheme, the non-linear terms are integrated explicitly and the linear terms (including the algebraic equations) are implicitly treated (see [30]).

The first sub-step gives an estimate A^* of the solution at $T + \Delta T$:

$$M_T(A^* - A^T) = \frac{\Delta T}{2} M_L(A^* + A^T) + \Delta T M_{NL} N L^T + M_{BC} A^* - BC(T + \Delta T),$$

and with this estimate we correct the integration of the nonlinear term in the second and final sub-step:

$$\begin{aligned} M_T(A^{T+\Delta T} - A^T) &= \frac{\Delta T}{2} M_L(A^{T+\Delta T} + A^T) + \frac{\Delta T}{2} M_{NL}(N L^{T+\Delta T} + N L^T) \\ &\quad + M_{BC} A^{T+\Delta T} - BC(T + \Delta T). \end{aligned}$$

Note that at every sub-step we have to solve the same linear system. This allows us to factorize the system matrix once at the beginning of the integration and then, at each sub-step, we have only to solve the factorized system. The simulation code has been programmed in MATLAB, and runs quite fast; it takes about 30 seconds in a standard 3GHz Pentium PC to advance 10000 time steps in a grid with 2000 spatial points.

In order to check that the code is actually second order in time and space we run the following test: in a domain with $L = 4$, and with $c_t = \frac{1}{2} + \frac{i}{2}$ and $c_r = \frac{1}{2} - \frac{i}{2}$, we send a pulse from the left side,

$$F_1(T) = e^{-(T-4)^2} \quad \text{and} \quad F_2(T) = 0,$$

and integrate the system with zero initial condition from $T = 0$ to $T = 10$ (the

final solution at $T = 10$ is quite involved as it can be seen in Fig 29). We perform the integration for three different temporal and spatial resolutions $\Delta X = \Delta T = .01, .01/2$ and $.01/4$. In Fig 31 we plot, using logarithmic scale, the differences between two successive solutions versus the spatial coordinate X at $T = 10$. It can be clearly appreciated that the ratio between the differences is 4, which indicates that the solution is second order, i.e., the error goes as $\sim \Delta X^2 + \Delta T^2$.

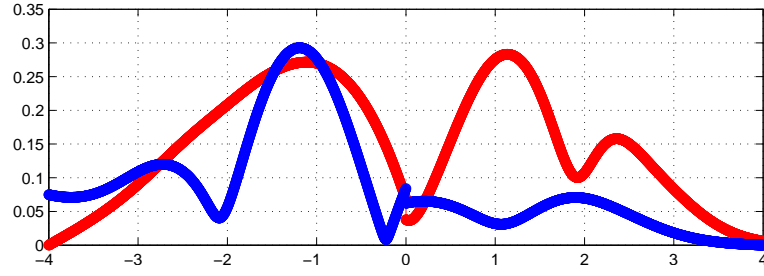


Figure 30: Spatial profiles of the solution at $T=10$: $|A^+|$ (blue line) and $|A^-|$ (red line).

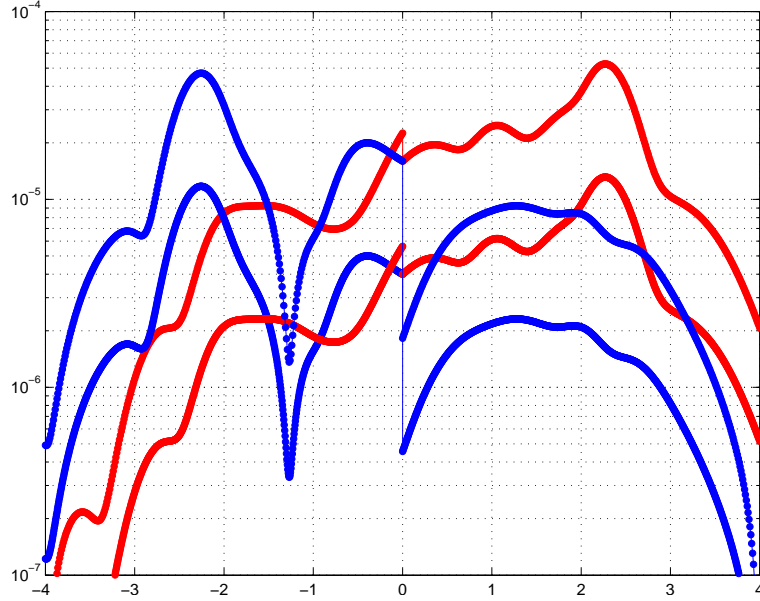


Figure 31: Modulus of the difference between two increasingly refined solutions at $T=10$. Blue line for A^+ and red for A^- .

Conclusions

In this report we have analyzed the weakly nonlinear dynamics of nonlinear light propagation in a FBG with a narrow defect. The problem has been first formulated in terms of two sets of NLCME that apply at both sides of the defect (regions 1 and 2 in Fig. 6) together with a jump condition at the location of the defect, see eqs. (41). The coefficients for the jump condition depend on the profile of the defect, and their computation requires to solve a scattering problem. This problem has been solved numerically for several representative defects in order to illustrate the relation between the defect shape and the resulting coefficients. From the standing GS exact solution we have constructed a general family of nonlinear defect modes that depend on the particular values of the coefficients of the jump condition. The defect modes correspond to persistent in time light distributions that remain spatially confined to the vicinity of the defect. The stability of these nonlinear defect modes has been analyzed numerically, and for two representative stable defect modes we have also explored the possibility of light pulse trapping (i.e., the possibility of exciting the standing defect modes by sending moving pulses to collide with them). A numerical code for the simulation of the temporal evolution of the complete problem of light propagation in a FBG with a narrow defect, eqs.(41), has been also implemented, and its details are described in this report. This numerical code is required for the study of the defect mode stability, and for the determination of the light trapping characteristics of the defects.

Some conclusions that can be drawn from this research project are now summarized below:

1. A narrow defect gives rise to a first order effect only if the distortion of the refraction index that it produces is comparable to the refraction index itself. In terms of the scaling of MLE eqs. (15) and (16), the size of the defect has to be of order 1, much larger than the amplitude of the grating, which is of the order of $\Delta n \ll 1$.
2. If the narrow defect has small amplitude, of the order of the grating amplitude, then its effect, in first approximation, is simply not felt. This looks surprising at first, but it makes perfect sense because if it were not so, every imperfection present in the small grating would produce a first order effect and, since there

are always imperfections due to manufacturing and wear, it would be impossible in practice to see any of the dynamics associated with periodic gratings.

3. The effect of a narrow defect is a jump of the envelopes along the characteristic lines of the hyperbolic NLCME. This has been previously modeled by adding Dirac-delta functions to the NLCME [16, 17, 18]. This formulation covers only the particular case of x -symmetric defects and, even in this case, it does not provide information about the relation between the defect shape and the resulting jump.
4. A family of nonlinear defect modes has been obtained by joining pieces of standing GS. This procedure was already used in [17], but the family that they derived was much more reduced because it only covered the particular case of symmetric defects with real transmission coefficient. We also show in this report that these more general defect modes that were not considered in [17] can be stable.
5. The formulation presented in this paper in terms of two sets of NLCME plus some jump conditions (see eqs.(41)) is also better suited for numerical computations than the previous Dirac-delta formulation used in [16, 17, 18]. The Dirac-deltas have to be approximated by introducing very high values of the functions at a very narrow region of the spatial grid, and this procedure is obviously problematic from the point of view of ensuring the order of accuracy of the numerical method. Our formulation has no problems of this kind since it is just composed of two sets of perfectly regular PDE's (which can be discretized in a completely straight forward way) together with some coupling boundary conditions that account for the jumps of the amplitudes at the defect.
6. The light pulse trapping characteristics of the defects have been also explored and, generally speaking, it has been found that while non-symmetric defects appear to just deflect the pulses without trapping any light, the symmetric defects always end up producing states with persistent trapped light at the defect.

Finally, it is interesting to mention that the formulation and the tools developed in this research project will surely be very useful for future studies on this problem. In

particular, they can be used to address a question that is very important from the technological point of view: how to design the internal profile of the defect in order to produce some prescribed light reflection or trapping properties.

References

- [1] G. P. Agrawal. *Nonlinear Fiber Optics*. Optics and Photonics. Academic Press, 1995.
- [2] Raman Kashyap. *Fiber Bragg Gratings*. Optics and Photonics. Academic Press, 1999.
- [3] Akira Hasegawa. *Optical Solitons in Fibers*. Springer Verlag, second edition, 1990.
- [4] C.M. de Sterke and J.E. Sipe. Gap solitons. *Progress in Optics*, XXXIII:203–260, 1994.
- [5] G. Kurizi, A.E. Kozhekin, T. Opatrný, and B. Malomed. Optical solitons in periodic media with resonant and off-resonant nonlinearities. *Progress in Optics*, 42:93–142, 2001.
- [6] A.B. Aceves. Optical gap solitons: Past, present and future; theory and experiment. *CHAOS*, 10(3):584–589, 2000.
- [7] X. Tr. Tran and N.N. Rosanov. Conservative and dissipative fiber bragg solitons. *Optics and Spectroscopy*, 105(3):393–435, 2008.
- [8] J.T. Mok, C.M. de Sterke, I.C.M. Littler, and B.J. Eggleton. Dispersionless slow light using gap solitons. *Nature Physics*, 2:775–780, 2006.
- [9] R.H. Goodman, R.E. Slusher, and M.I. Weinstein. Stopping light on a defect. *J. Opt. Soc. Am. B*, 19(7):1635–1652, 2002.
- [10] R.H. Goodman, R.E. Slusher, M.I. Weinstein, and M. Klaus. Trapping light with grating defects. In D. Clemence and G. Tang, editors, *Mathematical Studies in Nonlinear Wave Propagation*, pages 83–92. Am. Math. Soc., Providence, RI, 2005.
- [11] M.I. Weinstein. Resonance problems in photonics. In D. Hsieh, M. Zhang, and W. Sun, editors, *Frontiers in Applied mathematics, Proceedings of the 2nd International Symposium*. World Scientific, 2007.
- [12] R.H. Goodman and M.I. Weinstein. Stability and instability of nonlinear defect states in the coupled mode equations-analytical and numerical study. *Physica D*, 237:2731–2760, 2008.
- [13] T. Dohnal and A.B. Aceves. Optical soliton bullets in $(2+1)$ d nonlinear bragg resonant periodic geometries. *Studies in Appl. Math.*, 115:209–232, 2005.

- [14] T. Mayteevarunyoo and B.A. Malomed. Gap solitons in grating superstructures. *Optics Express*, 16(11):7767–7777, 2008.
- [15] R.H. Goodman, M.I. Weinstein, and P.J. Holmes. Nonlinear propagation of light in one-dimensional periodic structures. *J. Nonlinear Sci.*, 11:123–168, 2001.
- [16] W.C.K. Mak, B.A. Malomed, and P.L. Chu. Formation of a standing-light pulse through collision of gap solitons. *Phys. Rev. E*, 68(026609), 2003.
- [17] W.C.K. Mak, B.A. Malomed, and P.L. Chu. Interaction of a soliton with a local defect in a fiber bragg grating. *J. Opt. Soc. Am. B*, 20(4):725–735, 2003.
- [18] P.Y.P. Chen, B.A. Malomed, and P.L. Chu. Trapping bragg solitons by a pair of defects. *Phys. Rev. E*, 71(066601), 2005.
- [19] G. M. Webb M.P. Sørensen, M. Brio and J.V. Moloney. Solitary waves, steepening and initial collapse in the maxwell-lorentz system. *Physica D*, 170:287–303, 2002.
- [20] J. Kevorkian and J.D. Cole. *Multiple Scale and Singular Perturbation Methods*, volume 114 of *Applied Mathematical Sciences*. Springer-Verlag, 1996.
- [21] C.M Bender and S.A. Orszag. *Advanced Mathematical Methods for Scientists and Engineers*. Springer-Verlag, 1999.
- [22] C. Martel. Dispersive destabilization of nonlinear light propagation in fiber bragg gratings. *CHAOS*, 15:013701, 2005.
- [23] D.N. Christodoulides and R.I. Joseph. Slow bragg solitons in nonlinear periodic structures. *Phys. Rev. Lett.*, 62(15):1746–1749, 1989.
- [24] C.M. de Sterke. Theory of modulational instability in fiber bragg gratings. *J. Opt. Soc. Am. B*, 15(11):2660–2667, 1998.
- [25] H.B. Keller. *Numerical solution of two point boundary value problems*, volume 24 of *CBMS-NSF Regional Conferences in Applied Mathematics*. SIAM, 1976.
- [26] J. Cronin. *Differential Equations: Introduction and Qualitative Theory*, volume 180 of *Monographs and Textbooks in Pure and Applied Mathematics*. CRC Press, 1994.
- [27] A.B. Aceves and S. Wabnitz. Self-induced transparency solitons in nonlinear refractive periodic index. *Phys. Rev. Lett.*, 62:85–88, 1989.
- [28] I.V. Barashenkov, D.E. Pelinovsky, and E.V. Zemlyanaya. Vibration and oscillatory instabilities of gap solitons. *Phys. Rev. Lett.*, 80:5117–5120, 1998.

- [29] I.V. Barashenkov and E.V. Zemlyanaya. Oscillatory instabilities of gap solitons: a numerical study. *Comp. Phys. Comm.*, 126:22–27, 2000.
- [30] J.D. Lambert. *Numerical Methods for Ordinary Differential Systems: The Initial Value Problem*. John Wiley and Sons, 1995.

List of Symbols, Abbreviations, and Acronyms

χ	linear polarizability
Δn	grating strength
$\Delta T, \Delta X$	time step, spatial grid spacing
δ_d	length of the defect
γ	cubic Kerr effect coefficient
κ	rescaled grating strength in the NLCME
λ_g	grating period
μ_0	vacuum permeability
ω_k, ω	propagating light frequency
Ω_p, ω_p	characteristic frequency of the polarization response
σ	rescaled nonlinear coefficient in the NLCME
ε_0	vacuum permittivity
a, a', a_1, a_2	solutions of the defect scattering problem
A^\pm, A_1^\pm, A_2^\pm	slow envelopes of the light wavetrains
B	magnetic field
c	vacuum speed of light
c_t, c_r, c'_t, c'_r	transmission and reflection coefficients
D	dielectric displacement
E	electric field
$f(x)$	defect profile
k	propagating light wavenumber
L	spatial domain $[-L, L]$ for the numerical integration
n_0, n	bare fiber and FBG refractive index
P	polarization field
v_g	propagating light group velocity
x, t, X, T	spatial and temporal variable, fast and slow
x_∞	finite length for the numerical integrations
DM	Defect Mode
DM1, DM2	Defect mode families
FBG	Fiber Bragg Grating

GS	Gap Soliton
MLE	Maxwell Lorentz Equations
NLCME	Non Linear Coupled Mode Equations